The Institute for Solid State Physics
The University of Tokyo

Activity Report
2009

ISSP

Activity Report
2009

Contents
Pages

The center building is ISSP.

Preface

This booklet constitutes the annual Activity Report of the Institute for Solid State Physics (ISSP), the University of Tokyo for the academic year 2009.

ISSP was established in 1957 as a joint-use central research institution in the field of basic materials science. After its 40 years of operation at the Roppongi campus, ISSP relocated itself to a new campus in Kashiwa city and started afresh in April 2000. The relocation was a good occasion for renovation and upgrading of the research facilities and infrastructures. This Activity Report as well as those in previous years presents some of the research accomplishments of ISSP during the first 10 years in Kashiwa.

The start of the academic year 2010 is a turning point for ISSP in two senses. Firstly, it is the restart of ISSP as a joint-use/joint-research organization under a new scheme set by the Ministry of Education, Culture, Sports, Science and Technology (MEXT). Secondly, it is the start of the second term of the six-year mid-term for the national universities. The University of Tokyo under the leadership of President Junichi Hamada launched the Action Scenario for the coming years. ISSP sets the following objectives in the Action Scenario:

(1) ISSP plays its due role as a central joint-use/joint-research organization and as an international research hub in the field of basic material science.

(2) ISSP aims at discovery of new materials and new properties, development of materials science under extreme conditions, renovation of materials research with advanced beam probes, and promotion of theoretical and computational condensed matter science.

(3) ISSP contributes to nurturing of talents in state-of-art research environment.

During the past academic year, ISSP celebrated two inaugurations of long-awaited beam-line facilities. In October 2009, a new high-brilliance soft X-ray beam-line was put in operation at BL07LSU in SPring-8. In March 2010, joint construction with KEK of the High Resolution Chopper Spectrometer was completed at the neutron beam-line BL12 of J-PARC/MLF. In the International MegaGauss Science Laboratory, the d.c. motor generator is now in operation to produce non-destructive long-pulse high magnetic field. Together with the short-pulse megagauss field, the IMGSL constitutes a world center of high magnetic field. Other projects vigorously promoted in collaboration with the respective communities include, the Advanced Coherent Light Laboratory envisaged as a state-of-the-art facility of ultrafast, short-wavelength and high-peak-power lasers, and the Computational Materials Science Initiative planned in conjunction with the High Performance Computational Infrastructure (Next-Generation Supercomputer) Project.

June, 2010

Yasuhiro Iye
Director
Institute for Solid State Physics
The University of Tokyo

Behavior of the Xe-Fe System above the Metallization Pressure of Xenon

Yagi Group

The behavior of Xe-Fe system was investigated under ultra-high pressures by in situ X-ray diffraction measurements using a laser-heated diamond anvil cell. The so-called missing xenon problem is a long standing, unsolved problem. The Earth's atmosphere is depleted of helium and xenon, and more than 90% of the expected xenon is "missing" compared to the abundance in the original material of the Earth. Since helium is a light element it readily escapes from the Earth's gravitational field, but xenon is too heavy to escape. Therefore, the missing xenon is believed to be captured somewhere inside the Earth and various possible mechanisms for this have been discussed. Since the discovery that xenon becomes a metallic solid with an *hcp* structure above 120 GPa and that iron is also an *hcp* metal under the same conditions, theoretical studies have proposed that xenon could be trapped in the Earth's core by forming solid solutions or compounds with iron. So far, however, experiments have been performed only up to about 50 GPa and no studies have been reported at pressures above the metallization pressure of xenon. In this study, we investigated the behavior of the Xe-Fe system up to 155 GPa and 3000 K using a laser-heated diamond anvil cell and synchrotron X-ray radiation, and discussed the possibility for the solid solution in Xe-Fe system at Earth's core pressure [1].

Experiments were performed by high-pressure in situ X-ray diffraction using a laser-heated diamond anvil cell combined with synchrotron radiation. Beveled anvils with 100-300 μm culets were mainly used. Pure iron and a NaCl pellet, which works as a thermal insulator as well as a pressure marker, were placed in the gasket hole, together
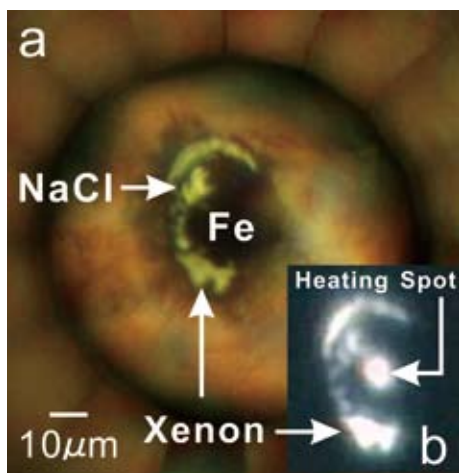

Fig. 1. Photographs of the sample chamber observed through the diamond anvil at 155 GPa. Insertion is a view observed during heating above 2000K. Xenon remains transparent even above the metallization and at 155 GPa during the heating.
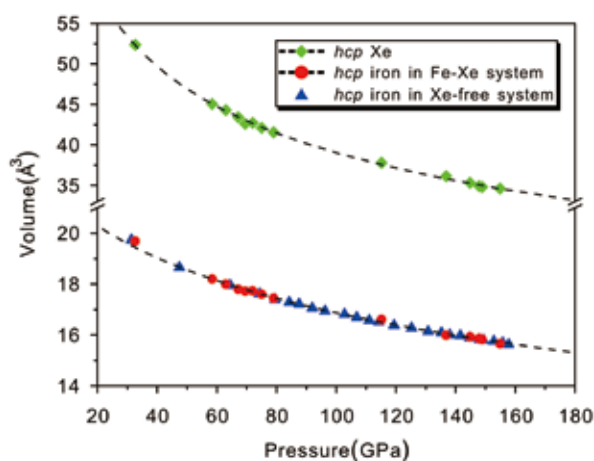

Fig. 2. Volume compression curves of *hcp* xenon and *hcp* iron observed at room temperature after the heating. No difference was observed between the volume of iron in two runs with or without xenon, which means no chemical reaction occurs at all between these two *hcp* metals.

with Xe with a purity of 99.999%. Loading of Xe was made cryogenically. Heating was conducted using focused fiber lasers from two sides of the sample so as to heat a 10-20 μm diameter spot. Figure 1 shows the sample chamber at 155 GPa and room temperature, together with that at 2000 K (insertion). Even above the metallization of Xe at about 120 GPa, it remains transparent in this thickness.

Angle-dispersive XRD measurements were conducted at high pressure and high/room temperature using the BL10XU beam line of the SPring-8. Clear diffractions of xenon, iron and NaCl were observed in the entire range of pressure and temperature and no additional diffraction was observed even after heating the samples to 3000 K at 155 GPa. This fact clearly indicates that no new compound was formed even under these extreme conditions. Figure 2 shows the volume compressions of *hcp* xenon and *hcp* iron observed at room temperature after the heating. Volume compressions of iron were repeated with and without xenon, and no difference of volumes were observed at all between them. This fact clearly indicates that no dissolution of xenon into iron occurred even though both of these two material became the same *hcp* metals. The unit cell volumes of the two *hcp* metals, xenon and iron, differ by more than 100% even at about 155 GPa, which means that the atomic sizes of these two metals differ more than 30%. This is probably the reason why no dissolution occurs in this system even after the metallization of xenon. Present results suggest that some mechanism other than the dissolution in the Earth's core has to be considered to solve the "missing xenon problem".

Reference
[1] D. Nishio-Hamane, T. Yagi, N. Sata, T. Fujita, and T. Okada, Geophys. Res. Lett. **37**, L04302 (2010).

Authors
D. Nishio-Hamane, T. Yagi, T. Fujita, T. Okada and N. Sata[a]
[a]IFREE, Japan Agency of Marin-Earth Science and Technology

Development of Space Efficient Opposed-Anvil High-Pressure Cell: Application to Optical and NMR Measurements up to 9 GPa

Takigawa, Yagi, and Uwatoko Group

Application of pressure often leads to the discovery of a new state of matters. In fact pressure-induced quantum phase transitions have been extensively studied in strongly correlated electron systems, such as transition metal oxides and heavy electron materials. Generally, however, one has to compromise between demands for larger sample space and higher pressure. Certain volume-sensitive experimental methods, such as nuclear magnetic resonance (NMR) providing microscopic information on ordering and fluctuations of correlated electrons, have been performed using a
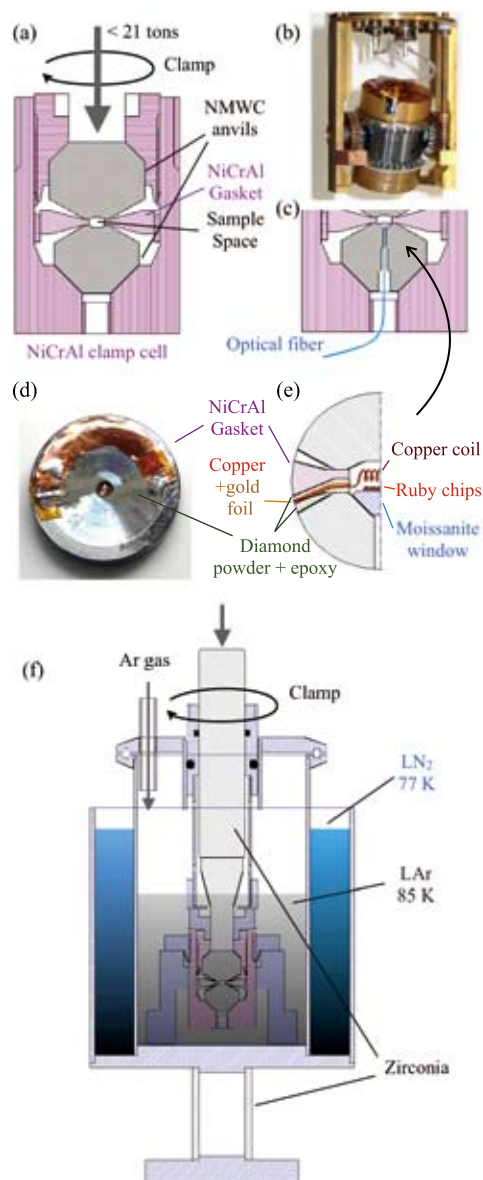

Fig. 1. (a) The cross sectional view of the high-pressure clamp cell. (b) The whole cell can be mounted on an geared two-axis goniometer for arbitrary alignment of the sample in magnetic field. (c) shows the setting for optical measurements, installed with a modified anvil attached with a moissanite (SiC) window and a optical fiber. (d) shows the NMR coil and wire setting on the gasket with the enlarged view shown in (e). (f) The cross sectional view of the argon loading system. Ar gas is liquified by the liquid nitrogen in the outer pot. Then the load is transmitted through the rod made of alumina-zirconia composite ceramics, which has low thermal conductivity.
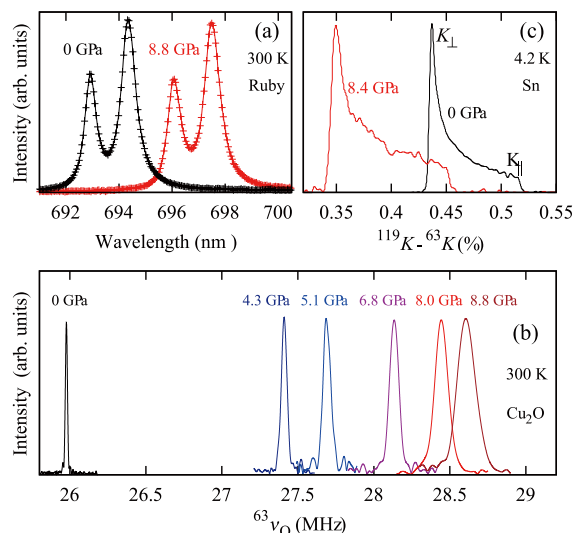

Fig. 2. Spectra of manometers at various pressure values in Ar medium. (a) Room temperature ruby fluorescence spectra at ambient pressure and at 8.8 GPa. (b) ^{63}Cu-NQR spectra of Cu_2O at 300 K. (c) ^{119}Sn-NMR spectra of metallic β-Sn at 4.2 K. Since β-Sn has a tetragonal crystal structure, the NMR spectra are broadened by the axial anisotropy of the Knight shift. The peak of the spectra represents the Knight shift for the field in the *ab*-plane.

piston-cylinder-type pressure cell equipped with sufficiently large sample space of the order of 100 mm^3. However, the upper pressure limit such a cell can reach is less than 4 GPa. On the other hand, much higher pressure beyond 10 GPa can be generated by a Bridgeman-type cell or a diamond-anvil-cell. But the available space is 1 mm^3 or less.

We have developed a new type of opposed-anvil pressure cell shown in Fig. 1, which can be used to generate pressure up to 9 GPa over a volume of 7 mm^3 with the total cell size of ϕ29mm $\times$ 41mm [1]. The pair of anvils is made of non-magnetic WC alloy (Fujilloy MF10). The gasket and the clamp cell are made of non-magnetic 56Ni-40Cr-4Al alloy. We have examined more than 40 different shapes and materials of gasket to optimize the available pressure and volume. Our cell has three advantageous features: (1) A transparent moissanite window can be attached for optical measurements (Fig. 1c). We measured the fluorescence from ruby for accurate determination of pressure. (2) The compact size of the cell allows arbitrary rotation of the whole cell by a two-axis goniometer to achieve precise alignment of a single crystal sample in a superconducting magnet (Fig. 1b). (3) We can use argon as the pressure transmitting medium. Ar is a soft molecular solid at high pressure, providing highly hydrostatic environment (Fig. 1f).

In order to establish the convenient pressure scale for NMR experiments, we have measured precise pressure and temperature dependences of the nuclear quadrupole resonance (NQR) frequency of Cu_2O and the NMR Knight shift of Pt and Sn metals. The pressure values are determined in-situ by the fluorescence from ruby as shown in Fig. 2. The sharp spectra in Fig. 2 indicate good homogeneity of the pressure. See the other article by Takigawa, Ohgushi, Yagi, and Uwatoko group in this report to see how powerful such a cell is in the actual NMR experiments.

References
[1] K. Kitagawa, H. Gotou, T. Yagi, A. Yamada, T. Matsumoto, Y. Uwatoko, and M. Takigawa, J. Phys. Soc. Jpn. **79**, 024001 (2010).

Authors
K. Kitagawa, H. Gotou, T. Yagi, A. Yamada, T. Matsumoto, Y. Uwatoko, and M. Takigawa

Spontaneous Formation of a Superconducting and Antiferromagnetic Hybrid State in SrFe$_2$As$_2$ under High Pressure

Takigawa, Ohgushi, Yagi, and Uwatoko Groups

Competition between magnetism and superconductivity is ubiquitous in unconventional superconductors such as cuprates, heavy fermions, and the recently discovered family of iron pnictide, indicating close relation between the magnetic interaction and the pairing mechanism. Unlike in cuprates, where the superconductivity is obtained by carrier doping (chemical substitution), some of the antiferromagnetic (AF) iron pnictide parent compounds become superconducting also by applying pressure. This enables us to investigate the phase diagram precisely, without being disturbed by disorder.

We have performed ^{75}As NMR experiments in SrFe$_2$As$_2$ under high pressure [1] using the newly developed space-efficient opposed-anvil pressure cell [2] (See the other article by Takigawa, Yagi, and Uwatoko group in this report). Figure 1 shows the temperature (T) dependence of $1/(T_1T)$ (the nuclear relaxation rate ($1/T_1$) divided by T) at various pressure values. For the pressure up to 4.2 GPa, $1/(T_1T)$ increases with lowering temperature towards the Néel temperature, where the simultaneous structural and antiferromagnetic (AF) transition takes place. At 5.4 GPa, however, the paramagnetic (PM) NMR signal persists down to the lowest temperature. The sudden drop of $1/(T_1T)$ marks the superconducting (SC) transition as confirmed by the Knight shift and the ac-susceptibility measurements. The phase diagram shown in the inset of Fig. 1 indicates that the SC phase, which coexists with the AF phase as described below, is limited to a narrow pressure range near 6 GPa. Such a fragile SC state as opposed to more stable SC states obtained
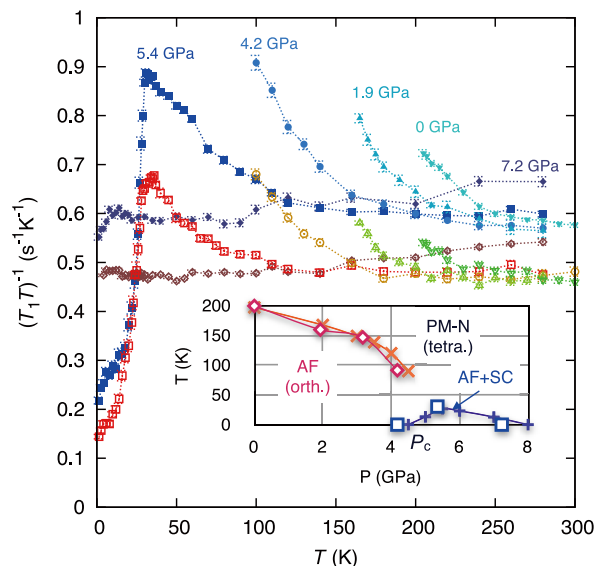

Fig. 1. The main panel shows the temperature dependence of $1/(T_1T)$ in the paramagnetic (PM) phase for the magnetic field perpendicular (colored in dark blue to sky blue) or parallel (colored in orange to green) to the c-axis. For the pressure up to 4.2 GPa, $1/(T_1T)$ increases with lowering temperature down to the Néel temperature, where the first-order transition from the tetragonal paramagnetic (PM) phase into the orthorhombic antiferromagnetic (AF) phase takes place. At 5.4 GPa, superconducting (SC) state appears below 30 K causing the rapid drop of $1/(T_1T)$. The finite value of $1/(T_1T)$ at the lowest temperature indicates a substantial residual density of states in the SC phase. Neither SC nor AF phase was observed at 7.2 GPa. The inset shows the phase diagram obtained from the present study (open symbol) and the results in ref.[3] (crosses).
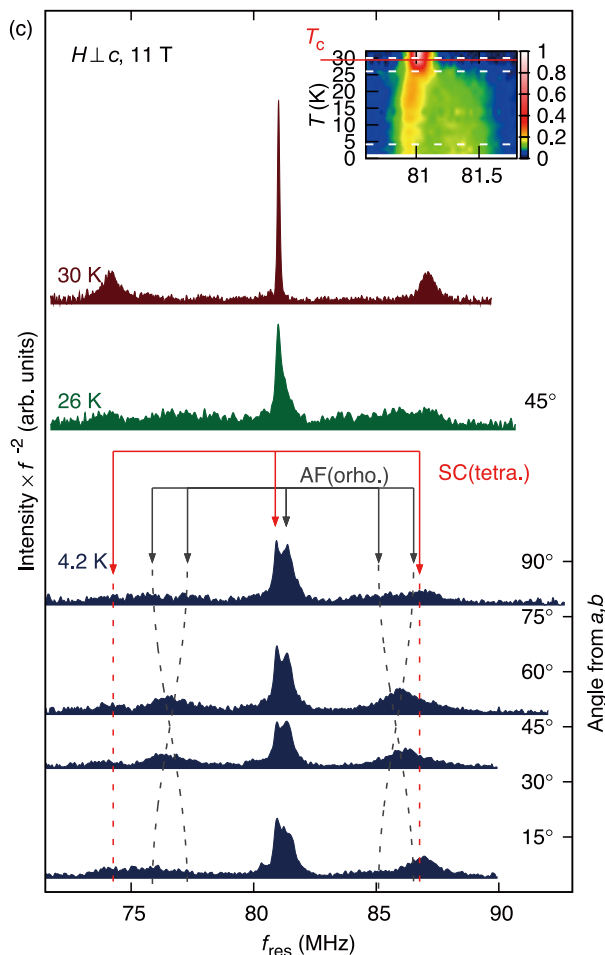

Fig. 2. The main panel shows the ^{75}As NMR spectra in the paramagnetic normal phase (30 K), and in the SC+AF coexisting phase (26 K and 4.2 K). The spectrum at 26 K, slightly lower than the SC+AF transition temperature, is significantly broadened due likely to incommensurate spin structure. The variation of the spectra at 4.2 K with the field direction in the ab-plane provides microscopic evidence for the coexistence of the tetragonal SC phase and the twinned orthorhombic AF phase. The color plot in the inset shows the temperature variation of the spectral intensity of the quadrupole split central line.

by carrier doping may be related to the compensated nature of the electron and hole Fermi surfaces.

The NMR spectra at low temperatures provide microscopic evidence for the coexistence of the SC and AF phases. For the field along the c-axis, the NMR spectrum consists of a set of quadrupole split three resonance lines from paramagnetic SC domains and a pair of such sets split by the hyperfine field from the stripe-type AF domains (not shown). Figure 2 shows the variation of the NMR spectra with temperature for the field in the ab-plane. In this case, the spectrum from the AF domains does not split but largely shifts by the hyperfine field. The spectrum at 4.2 K provides unambiguous evidence that the tetragonal SC phase coexists with the orthorhombic AF phase. We should emphasize that there is a single phase transition near 30K, below which the entire sample goes into the SC+AF coexisting phase. Thus the coexistence of two different orders should not be due to extrinsic inhomogeneity. The SC and AF domains are likely to form a nano-scale hybrid structure, which has not been seen in any other class of materials.

References
[1] K. Kitagawa, N. Katayama, H. Gotou, T. Yagi, K. Ohgushi, T. Matsumoto, Y. Uwatoko, and M. Takigawa, Phys. Rev. Lett. **103**, 257002 (2009).
[2] K. Kitagawa, H. Gotou, T. Yagi, A. Yamada, T. Matsumoto, Y. Uwatoko, and M. Takigawa, J. Phys. Soc. Jpn. **79**, 024001 (2010).

[3] K. Matsubayashi, N. Katayama, K. Ohgushi, A. Yamada, K. Munakata, T. Matsumoto, and Y. Uwatoko, J. Phys. Soc. Jpn. **78**, 073706 (2009)

Authors
K. Kitagawa, N. Katayama, H. Gotou, T. Yagi, K. Ohgushi, T. Matsumoto, Y. Uwatoko, and M. Takigawa

Sign-Reversal of Field-Angle Resolved Specific Heat Oscillations in a Heavy Fermion Superconductor CeCoIn$_5$ and k_x^2-k_y^2 Pairing Symmetry

Sakakibara Group

Heavy-electron superconductors mostly have anisotropic gap functions which vanish (have nodes) for certain directions in the momentum space. Since the nodal structure is closely related to the pairing mechanism, its experimental determination is very important. To identify the gap structure is, however, a formidable task. Here we address the directional thermodynamic measurements. In anisotropic superconductors, low energy spectrum of the quasiparticles in the vortex state much depends on the nodal structure. In particular, the electronic specific heat (C) has been demonstrated to exhibit a characteristic dependence on the angle between the field and the nodal directions [1]; in a low temperature "semiclassical" regime, C takes maxima (minima) when a magnetic field H is oriented along the antinodal (nodal) directions. This effect allows one to probe the nodal structures experimentally. We have been investigating the anisotropic gap structures of heavy-electron superconductors by means of field-angle dependent specific heat (C_θ) measurements [2].

In the heavy fermion superconductor CeCoIn$_5$ (T_c = 2.3 K),

our previous C_θ measurements ($H \perp c$) performed down to 300 mK (T/T_c=0.13) revealed a clear fourfold oscillation with minima along [100] directions [3]. A naive interpretation of the results infers that the nodal direction is [100] ($k_x k_y$ symmetry), which is contrary to other various experiments on CeCoIn$_5$ including the field-orientation dependent thermal conductivity measurements [4] where k_x^2-k_y^2 symmetry is deduced. Very recently, C_θ of d-wave superconductors has been studied theoretically in a wide H-T region [5]. It has been pointed out that applying H along the gap nodes may result in maxima of C_θ in an intermediate-T region. That is, the anisotropy of C_θ changes sign at a low temperature T/T_c~0.1 [5]. If this would be the case for CeCoIn$_5$, then our previous C_θ data would be interpreted in terms of k_x^2-k_y^2 symmetry. In order to explore this possibility, we extended the C_θ measurements on CeCoIn$_5$ to lower T down to 120 mK using a dilution refrigerator [6]. The magnetic field was rotated in the ab plane, covering from [100] through [010] directions.

We observed a fourfold angular oscillation of C_θ which can be expressed in a form $C=C_0+C_H(1-A_4\cos4\theta)$, where C_0 and C_H denote the field independent and dependent part of the specific heat, respectively, and θ is the angle of H measured from the [100] direction. Figure 1 shows a contour plot of the observed fourfold amplitude A_4 in the H-T plane, where H and T are reduced by H_{c2}=11.5 T and T_c. In a blue-colored region, A_4 is positive and C_θ takes minima along [100] directions, in full agreement with our previous experiment [3]. On cooling below 200 mK, we did observe a sign change in A_4 as shown in the figure. The sign reversal in A_4 is observed only at very low fields ($H \leq 0.15H_{c2}$). The crossover temperature of the sign reversal well agrees with the theoretical prediction, indicating that, for the first time, the low-temperature semiclassical region is reached experimentally [6]. In this region, C_θ takes minima along the [110] nodal directions, implying unambiguously that the gap symmetry of CeCoIn$_5$ is k_x^2-k_y^2.

References
[1] I. Vekhter *et al*., Phys. Rev. B **59**, R9023 (1999).
[2] T. Sakakibara *et al*., J. Phys. Soc. Jpn. **76**, 051004 (2007).
[3] H. Aoki *et al*., J. Phys.: Condens. Matter **16**, L13 (2004).
[4] K. Izawa *et al*. Phys. Rev. Lett. **87**, 057002 (2001).
[5] A.B. Vorontsov and I. Vekhter, Phys. Rev. B **75**, 224501 (2007).
[6] K. An *et al*., Phys. Rev. Lett. **104**, 037002 (2010).

Authors
K. An, T. Sakakibara, R. Settai[a], Y. Onuki[a], M. Hiragi[b], M. Ichioka[b], and K. Machida[b]
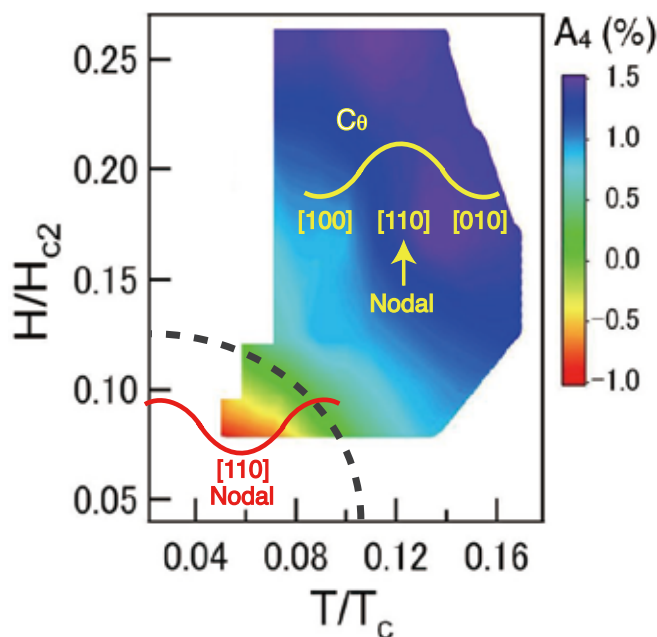[a] Osaka University
[b] Okayama University

Fig.1. Contour plot of the fourfold amplitude $A_4(T,H)$ of CeCoIn$_5$ obtained by the field-angle resolved specific heat (C_θ) measurements. In the high-T and high-H (blue colored) region, C_θ takes minima along the aninodal ([100]) directions. On entering the semiclassical region bounded by the dashed line, C_θ changes the sign of the oscillation and takes minima along the nodal ([110]) directions. From these observations, the gap symmetry of CeCoIn$_5$ was confirmed to be k_x^2-k_y^2.

Narrow Band Noise in Charge-Ordered Molecular Conductor β-(BEDT-TTF)$_2$PF$_6$

Mori Group

Recently, in the field of molecular conductors, "charge-ordering (CO)", where Coulomb interactions between conduction electrons play important roles, has been intensively studied from theoretical and experimental points of view. Since Coulomb repulsion energy competes with kinetic energy of conduction electrons, the electronic state transforms from itinerant conditions such as metallic states to localized ones like short or long-range charge-ordered states,
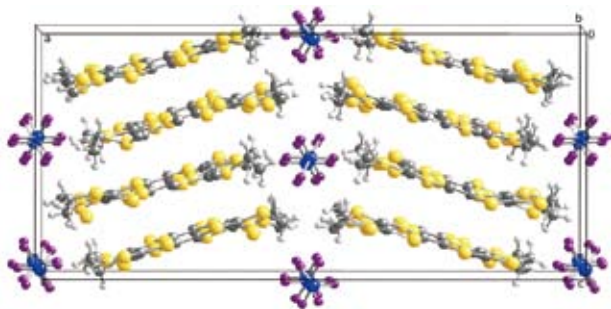
Fig. 1. Crystal structure of β-(BEDT-TTF)$_2$PF$_6$ at 128 K, where the c'-axis (300 K) is doubled to the b-axis (128 K) due to the charge-ordering below 297 K.

frequently with metal-insulator (MI) transitions accompaying lattice distortions in lowering temperatures. We have explored novel electronic states by applying external stimuli not only like temperature and pressure, but also of electric and magnetic fields for charge-ordered molecular materials. As for electric field, the giant nonlinear conductions, the thyristor effect [1], and the electric-field induced metastable state [2] for charge-ordered molecular conductors have been investigated. These responses, however, have been observed at low temperatures around 4 - 70 K. The system operated at room temperature should be developed in order to clarify the electronic states under the external stimuli and to make a potential towards organic electronics.

In this research, the electric-field response of β-(BEDT-TTF)$_2$PF$_6$ [3] (Fig. 1) have been investigated. This salt has the MI transition around room temperature, T_{MI} = 297 K, induced by the CO, below which the superlattice (0, 0, 1/2) has grown. In this article, the nonlinear conduction at room temperature and the sample voltage oscillation at 1 – 3 kHz in the audible range below 260 K by applying dc current are reported.

The single crystals of β-(BEDT-TTF)$_2$PF$_6$ were prepared by electrocrystallization method of BEDT-TTF (70 mg) and TBA·PF$_6$ (700 mg) with applying constant current of 0.25 µA in distilled 1,1,2-trichloroethane (100 mL) at 303 K above T_{MI} in the period of 4 months. The temperature dependence of resistivity is measured by pseudo two-probe method with utilizing carbon paste as contacts. The current driven E-J characteristics were measured by two-probe method with 5 - 50 msec pulse and 1 sec duration time from 291 – 218 K. The length of carbon contacts is 75 µm. The time dependences were monitored by oscilloscope.

The temperature dependence of resistivity with pseudo-four probe method for β-(BEDT-TTF)$_2$PF$_6$ was measured; the resistivity along the a' axis was larger than that along the c' axis by a half to one order of magnitude. The transitions due to the CO were observed around 295 K both along the a'- and c'-axes. The current driven E-J characteristic with applying 5 ms pulse and 1 sec duration time along the a'-axis was also measured; the nonlinear conduction was observed at 291.4 K, the negative differential resistance (NDR) was revealed below 273.1 K, and sharp voltage drop was demonstrated below 262.2 K. In the region of voltage drop, voltage oscillation was observed by an oscilloscope. At 230 K, the sample voltage decreased by applying 50 msec dc current of 1.77 Acm^{-2}, the voltage oscillation started for 12 msec under 1.79 Acm^{-2}, continued for 30 msec under 1.81 Acm^{-2}, and developed for 50 msec above 1.86 A cm^{-2} (Fig. 2). After that, the oscillation started to decrease by applying 2.15 Acm^{-2} and disappeared under 2.16 Acm^{-2}. The Fourier transformed spectra at 230 K revealed the fundamental frequency f_1 with 1 – 3 kHz and harmonic frequency f_2 - f_5 as shown in Fig. 3.

The frequency f_1 - f_5 was proportional to the applied current density J Acm^{-2} at 230 K. The linear relationship was reminiscent of CDW (charge density wave) or SDW (spin density wave) slidings of one-dimensional (1D) conductors. The ratio of J_{CDW} / f_1 in CDW movement for 1D conductor NbSe$_3$ was as follows;

$$\frac{J}{f_1} = Nne\lambda_0 \qquad (1)$$

J is current density, f_1 is fundamental frequency, n is calculated carrier density by material stoichiometry, Nn is observed carrier density, e is electron charge, λ_0 is period of CDW corresponding to a lattice parameter. The value N is close to 1 for one-dimensional CDW materials. On the other side, n = 4 / V_{cell} = 4 / 3254.6 Å^{-3}, N seems to be 2-5, and λ_0 is the lattice parameter a for β-(BEDT-TTF)$_2$PF$_6$. The current density dependence of frequency f_1 from 246.2 K to 221.6 K and temperature dependence of N are calculated, respectively. With lowering temperatures, N increases from 2 to 5, indicating that the excitation occurs coherently from 2 charge-ordered chains to 5 ones.

In conclusion, the narrow band noise in the collective excitation of the CO for psudo 2D molecular material β-(BEDT-TTF)$_2$PF$_6$ is observed below 260 K close to room temperature. It is characteristic that the fundamental frequency f_1 is comparatively low in the audible range
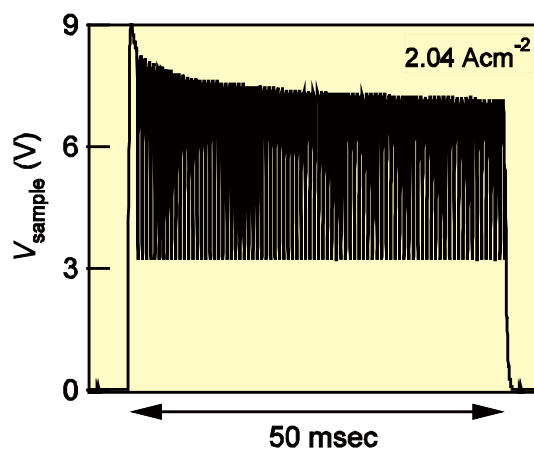

Fig. 2. V_{sample} oscillation under applied dc current 1.86 Acm^{-2} at 230 K for β-(BEDT-TTF)$_2$PF$_6$.
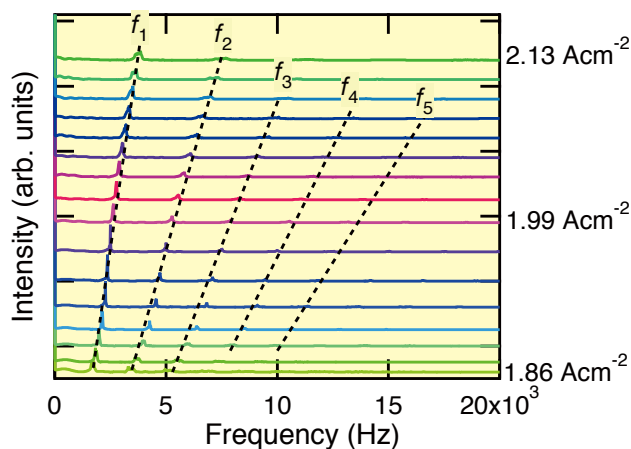

Fig. 3. Frequency dependence of oscillation spectra under various current densities at 230 K for β-(BEDT-TTF)$_2$PF$_6$. The Fourier transformed frequency increases proportionally to the applied dc current, suggesting the narrow band noise in the collective excitation of the charge order.

from 1 – 3 kHz and disappears suddenly above the threshold current, which might be related to the melting of CO state.

References
[1] F. Sawano *et al.*, Nature **437**, 522 (2005).
[2] S. Niizeki *et al.*, J. Phys. Soc. Jpn. **77**, 073170 (2008).
[3] H. Kobayashi *et al.*, Chem. Lett. 581 (2008); Y. Nogami *et al.*, J. Phys. IV France **12**, Pr9-233 (2002); Y. Ding *et al.,* Phys. Rev. B **69**, 115121 (2004).

Authors
T. Asano, A. Ichikawa, K. Takahashi, and H. Mori

Magnetic Torque Measurements on PTMA$_{0.5}$[Fe (Pc)(CN)$_2$]·CH$_3$CN: The Origin of Spontaneous Magnetization in [Fe(Pc)(CN)$_2$] Molecular Conductors

Tajima Group

The charge-transfer salts of [Fe(Pc)(CN)$_2$] are one-dimensional molecular conductors that exhibit giant negative magnetoresistance (GNMR) [1]. Here, Pc denotes phthalocyanine. This GNMR is an interesting phenomenon, since it is not caused by a sharp transition such as the field-induced metal-insulator transition. It is highly anisotropic for the magnetic field direction, reflecting molecular orientation of [Fe(Pc)(CN)$_2$].

Recently we have measured the magnetic torque and heat capacity of TPP[Fe(Pc)(CN)$_2$]$_2$ salt and analyzed them together with magnetic susceptibility data [2]. Our study revealed that: i) the peak in the magnetic susceptibility data around 25 K is due to the antiferromagnetic short-range order of *d*-electrons; ii) π electrons fall into an antiferromagnetic state below 13 K, with fluctuations of state appearing even at 17 K; and iii) an anomalously large spin-flop field (80 kOe at 9 K) is observed for the π-electron antiferromagnetic state. However, the origin of the spontaneous magnetization due to the parasitic ferromagnetism had not been clarified. This phenomenon is commonly observed in all the conducting salts of [Fe(Pc)(CN)$_2$] around 6 K. Very recently, we have proposed the charge-ordered ferrimagnetism in the π electron system as the possible origin of the parasitic ferromagnetism [3]. In this paper, we report the summary of the
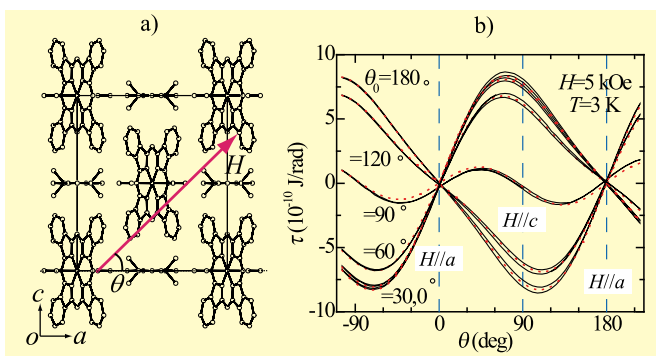

Fig. 1. (a) The definition of the field direction and crystal structure of PTMA$_{0.5}$[Fe(Pc)(CN)$_2$]·CH$_3$CN. (b) Magnetic torque curves at 3 K for the field of 0.5 T rotated within the *ac*-lane. In this measurement, the magnetic field of 40 kOe was applied at 10 K along the direction of θ = θ$_0$, and the sample was cooled down to 3 K in the same field. Torque curves were measured in the reduced field of 5 kOe. Black solid lines illustrate the observed data of torque curves, while the red dotted lines are the fit of Eq. (1) to the solid lines.
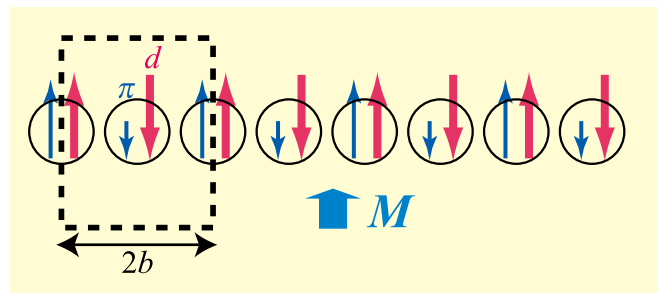

Fig. 2. The charge-ordered-ferrimagnetism model, which explains the parasitic ferromagnetism in [Fe(Pc)(CN)$_2$] salts.

study.

Figure 1a shows the crystal structure of PTMA$_{0.5}$[Fe(Pc)(CN)$_2$]·CH$_3$CN (*Pnnm*: *a*=13.900 Å, *b*=7.332 Å, *c*=16.317 Å, *Z*=1) [3] and the angle θ, which defines the magnetic field direction. The starting point of θ is parallel to the *a* axis. The [Fe(Pc)(CN)$_2$] molecules form a one-dimensional chain along the *b* axis. The point of this structure is that the projection of the CN axis in [Fe(Pc)(CN)$_2$] onto the *ac* plane is parallel to the *a*-axis. Since the magnetic easy axis in a [Fe(Pc)(CN)$_2$] salt should be parallel to the CN axis [2,4], we can postulate the possible origin of the parasitic ferrimagnetism, once the direction of the spontaneous magnetization is determined. Then we have determined the direction of spontaneous magnetization based on the torque measurements.

Figure 1b shows the magnetic-torque curves measured at 3 K, where spontaneous magnetization appears. In this measurement, a magnetic field of 40 kOe was applied at 10 K along the direction of θ = θ$_0$, and the sample was cooled down to 3 K in the same field. Then a torque curve was measured in the reduced field of 5 kOe. The black solid lines illustrate the observed data of the torque curves, and the red dotted lines are the fits of

$$\tau(\theta) = P \sin\theta + Q \sin2\theta \qquad (1)$$

to the solid lines. In this equation, the first and second terms represent the ferromagnetic and paramagnetic contributions, respectively. As can be seen from the figure, the solid lines are well reproduced by this equation. The paramagnetic contribution, *Q*, is ~1.5×10^{-10} J/rad in all the curves, while the ferromagnetic contribution, *P*, is positive for θ$_0$ > 0, negative for θ$_0$ < 180°, and approximately zero at θ$_0$ = 90°. This result indicates that a permanent magnetic moment due to spontaneous magnetization is formed along the *a* axis.

Since PTMA$_{0.5}$[Fe(Pc)(CN)$_2$]·CH$_3$CN is a *d*-π system, both *d* and π electrons can cause parasitic ferromagnetism associated with an antiferromagnetism. However, we can safely infer that the easy axis of the antiferromagnetism should be parallel to the CN axis of [Fe(Pc)(CN)$_2$] in either case. Thus, the result of Fig. 1b indicates that the direction of the spontaneous magnetization is parallel to the easy axis (= CN axis) in this salt. This conclusion explicitly rules out canted ferromagnetism as the origin of the spontaneous magnetization in this salt. It also excludes the possibility that the spontaneous magnetization is a parasitic ferromagnetism associated with the antiferromagnetism of Fe(III) *d*-electrons, since canted ferromagnetism is the only possible way for localized *d* electrons with *S* = 1/2 spin to develop parasitic ferromagnetism.

In the case of π electrons having delocalized character, there is another possibility. Considering the possible charge order suggested by several experiments [5,6], we have

proposed the charge-ordered-ferrimagnetism model shown in Fig. 2. In this model, an antiferromagnetic order of Fe(III) d spins coexists with that of π spins. Both have $4k_F$ periodicity ($2b$ in the real space for PTMA$_{0.5}$[Fe (Pc)(CN)$_2$]·CH$_3$CN). Since π spins are slightly charge ordered with $4k_F$ periodicity ($2b$), parasitic ferromagnetism appears for the direction parallel to the a axis (easy axis). This is a kind of ferrimagnetic order. However, the charge-rich and -poor sites are not fixed in this ferrimagnetic state.

References
[1] N. Hanasaki *et al.*, Phys. Rev. *B* **62**, 5839 (2000).
[2] H. Tajima *et al.*, Phys. Rev. B **78**, 064424 (2008).
[3] H. Tajima *et al.*, Phys. Rev. B **80**, 024424 (2009).
[4] N. Hanasaki *et al.*, J. Phys. Soc. Jpn. **72**, 3226 (2003).
[5] N. Hanasaki *et al.*, J. Phys. Soc. Jpn. **75**, 104713 (2006).

Authors
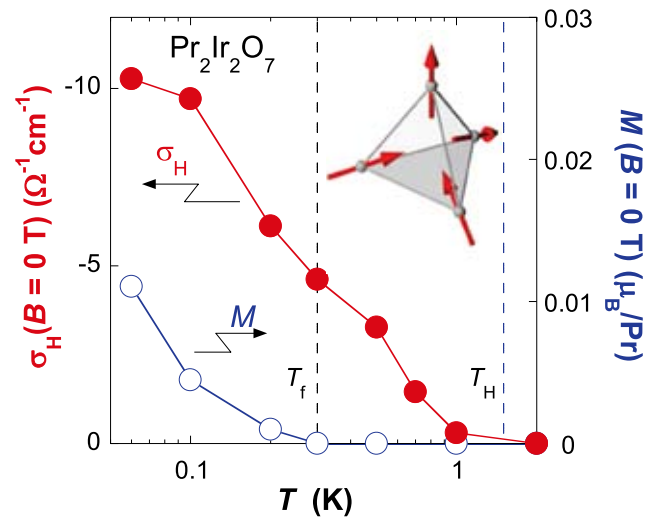H. Tajima, G. Yoshida, M. Matsuda, and J. Yamaura

Fig. 1. Temperature dependence of the remnant Hall conductivity $\sigma_H(B=0)$ (left axis) and remnant magnetization $M(B=0)$ (right axis) at zero field, obtained after a field sweep down from 7 T in the hysteresis loop measurements of the pyrochlore oxide Pr$_2$Ir$_2$O$_7$. Inset: unit of the pyrochlore lattice "2-in, 2-out" configuration of four <111> Ising spins on a tetrahedron.

Spontaneous Hall Effect as Evidence of Hidden Time-Reversal Symmetry Breaking in a Frustrated Magnet

Nakatsuji and Sakakibara Groups

The anomalous Hall effect (AHE) is a fundamental transport phenomenon where the electric current generates the transverse voltage drop in the normal plane to the spontaneous magnetization M in ferromagnets. This issue has attracted revived interest because of its topological and dissipationless character, and its potential application in spintronics. In particular, it has been shown that the intrinsic mechanism of the AHE can capture the dominant part in moderately dirty metals. This intrinsic AHE can be understood in terms of the adiabatic motion of the Bloch electrons under the electric field E, which acquire a quantum geometrical phase, the Berry-phase curvature b_{nk}, in the wavevector (k) space because of the relativistic spin-orbit interaction and the spin magnetization. This b_{nk} acts as a *fictitious magnetic field* in the k space and bends the orbital motion of electrons as in the case of the Lorentz force due to the real magnetic field B. Thus, it causes the AHE characterized by the finite Hall conductivity σ_H at $B = 0$.

Notably, the condition for observing the AHE at $B = 0$ is the *macroscopically* broken time reversal symmetry (T), which ensures a nonzero average of b_{nk} over the occupied Bloch states. It does not necessarily require a finite ferromagnetic spin alignment, but a noncoplanar spatial distribution of spins. Unconventional scenarios directly relying on a noncoplanar spin texture with the uniform scalar spin chirality have been addressed for ferromagnets. The macroscopically broken time-reversal symmetry and a resultant nonzero σ_H in the absence of a uniform spin magnetization have also been proposed in antiferromagnetic (AF) states and spin-liquid states with the scalar spin chirality. In this exotic example of a chiral spin-liquid, the uniform scalar spin chirality shows the long-range order (LRO), but the spin magnetic moment does not. However, the AHE at zero field has never been observed to date in the absence of the uniform spin magnetization associated with the ferromagnetism or the spin freezing.

We have recently discovered the macroscopically T broken spin-liquid state in a metallic magnet [1]. In particular, we observe the spontaneous Hall effect in the geometrically frustrated Kondo lattice Pr$_2$Ir$_2$O$_7$ even above its spin freezing temperature $T_f \sim 0.3$ K. A clear hysteresis is observed in the Hall conductivity around zero field below the onset temperature $T_H \sim 1.5$ K, whereas that in the magnetization curve appears only below T_f within an experimental accuracy. Namely, a large anomalous Hall conductivity σ_H is found even at zero field where the magnetization practically vanishes (Fig. 1), in sharp contrast to the conventional AHE in ferromagnets. This indicates an emergence of a hidden order at T_H that macroscopically breaks the time reversal symmetry without invoking a LRO of dipolar spins. The phenomenon may be understood in terms of a formation of the uniform spin chirality out of "2-in, 2-out" configurations (inset of Fig. 1) of localized magnetic moments of Pr^{3+} ions in an analogy to spin-ice systems.

Reference
[1] Y. Machida, S. Nakatsuji, S. Onoda, T. Tayama, and T. Sakakibara, Nature **463**, 210 (2010).

Authors
S. Nakatsuji, Y. Machida, S. Onoda[a], T. Tayama, and T. Sakakibara,
[a] Condensed Matter Theory Laboratory, RIKEN

Superconductivity in Hg$_x$ReO$_3$

Ohgushi Group

We have synthesized a new rhenium-based hexagonal bronze Hg$_x$ReO$_3$, which exhibits superconductivity with the transition temperature $T_c = 7.8$ K. This compound is not only a superconductor with the highest T_c among hexagonal bronzes, but also presents the novel crystallographic feature that Hg$_2^{2+}$ polycations are incorporated into open tunnels.

We grow polycrystalline Hg$_x$ReO$_3$ by using a cubic-anvil-type high-pressure apparatus. The x-ray diffraction profiles for the products are well described by the hexagonal bronze structure shown in Fig. 1(a). However, the chemical analysis gives the apparently anomalous result that $x = 0.44$,
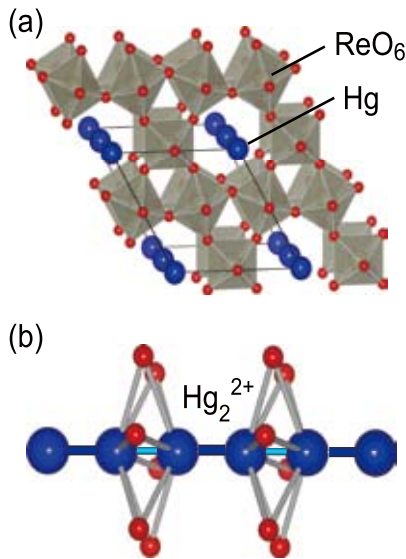
(a)

ReO$_6$

Hg

(b)

Hg$_2^{2+}$

Fig. 1. (a) Crystal structure of the hexagonal bronze Hg$_{2/3}$ReO$_3$, which is composed of corner-shared ReO$_6$ octahedra and Hg polycations in the open tunnels. The solid line shows a primitive unit cell. (b) Coordination environment of an Hg$_2^{2+}$ polycation.
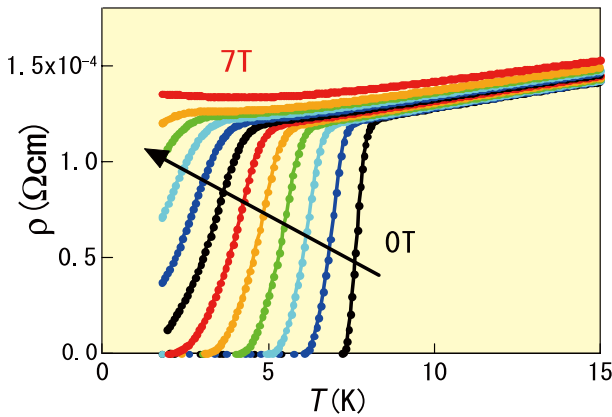

Fig. 2. Temperature (T) dependence of the resistivity (ρ) for Hg$_x$ReO$_3$. The magnetic field is applied perpendicular to the current direction.

which greatly exceeds the stoichiometric value 1/3 in the known hexagonal bronzes. This paradox can be resolved by assuming that the Hg$_2^{2+}$ polycations are incorporated into the tunnels (Fig. 1(b)) in contrast to A^+ monatomic cations in a conventional hexagonal bronze A_xBO_3, and that there is an Hg deficiency from the stoichiometric composition $x = 2/3$. Hg$_x$ReO$_3$ is a unique compound, in which the open-tunnel structures accommodate polyatomic cations.

Figure 2 represents the electrical resistivity of Hg$_x$ReO$_3$. The resistivity drops to zero at low temperature, indicating the onset of superconductivity. The Meissner signal detected by a SQUID magnetometer confirms that this superconductivity has a bulk nature. The T_c estimated from the midpoint of the resistivity drop is 7.8 K, which, to the best of our knowledge, is the highest T_c among the known hexagonal bronze superconductors; the highest T_c in hexagonal tungsten bronzes is 7.5 K in Rb$_x$WO$_3$, which was initially discovered in 1965 [1, 2]. The mechanism of high-T_c superconductivity in Hg$_x$ReO$_3$ is still unclear; however, a close inspection of the specific heat suggests the importance of the low-lying phonons related to Hg$_2^{2+}$ polycations (rattling phonons). The new rhenium-based superconductor Hg$_x$ReO$_3$ inspires a full reinvestigation of the interplay between the framework electrons and guest ions in the hexagonal bronze structure.

References
[1] A. R. Sweedler, C. J. Raub, and B. T. Matthias, Phys. Lett. **15**, 108 (1965).
[2] R. K. Stanley, R. C. Morris, and W. G. Moulton, Phys. Rev. B **20**, 1903 (1979).

Authors
K. Ohgushi, A. Yamamoto[a], Y. Kiuchi, and H. Takagi[a]
[a]RIKEN

Effects of Anharmonicity in 1-D Electron-Phonon System

K. Ueda Group

There is a growing interest in the effects of anharmonicity of ion vibrations. Experimentally superconductivity was found in β-pyrochlore compounds and it seems that anharmonic ion vibrations are responsible both for their superconductivity as well as some of unusual properties in the nomal phase. Recent experiments on NMR of KOs$_2$O$_6$ show that the NMR relaxation rate is dominated by the vibrations of K ions in the cages of OsO network. Such ion vibrations confined in cages are called rattling modes. The unusual temperature dependence of the NMR relaxation rate is explained by the effects of rattling modes [1].

Even if the ion vibrations are well localized they are coupled each other via electron-phonon couplings and/or phonon-phonon couplings. Concerning the latter couplings between the localized phonons and extended ones are considered. As a first step to study effects of the former type of couplings we have studied the one dimensional Holstein model with anharmonicity [2]. In the Holstein model the ion-electron coupling is given through the modulation of energy level of the electron orbitals. Therefore in this model A$_1$ mode of ion vibrations is considered.

Concerning the standard Holstein model without the anharmonicity, a consensus has been built that the ground state is always the dimerized CDW state for the spinless case while there is a phase transition between the metallic state and the dimerized CDW state at a finite coupling constant. We have studied the model with the anharmonicity by using the determinant quantum Monte Carlo Simulations.

The obtained ground state phase diagram is shown in Fig. 1. One can see that the anharmonic quartic term tends to stabilize the metallic phase, while the anharmonicity repre-
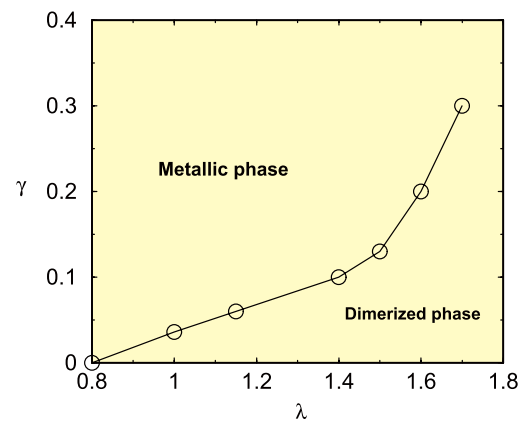

Fig. 1. Phase diagram of the one-dimensional spinful Holstein model with anharmonicity in the (λ,γ)-plane where λ is an electron-phonon coupling constant and λ is the coefficient of the quartic term of the potential.

sented by the negative quadratic term, a double well potential, favors the dimerized CDW phase. Studies on charge and spin correlation functions reveal that the metallic phase is a Luther-Emery liquid with gapless charge excitations and gapful spin excitations. In the dimerized CDW phase both spin and charge excitations are gapful.

References
[1] T. Dahm and K. Ueda, Phys. Rev. Lett. **99** 187003 (2007).
[1] J. Zhao and K. Ueda, to be published in J. Phys. Soc. Jpn (2010).

Authors
J. Zhao and K. Ueda

Anomalous Structural Change Induced by Strong Electron Exchange-Correlation in an Expanded Liquid Alkali Metal

Takada Group

One of the central issues in condensed matter physics is to understand the strong exchange-correlation (XC) effect between electrons which may cause some kinds of attraction related to a variety of phenomena such as superconductivity, ferromagnetism, and Wigner crystallization. Besides those kinds of attraction, the XC effect always acts as an attraction in the symmetric Landau's Fermi-liquid interaction for the entire region of the electron density n; this attraction increases monotonically with decreasing n, leading to a strong tendency toward electronic phase separation, which is, however, prohibited from developing macroscopically by the charge neutrality.

An expanded liquid alkali metal is an interesting system in which the latter attraction plays an essential role in not
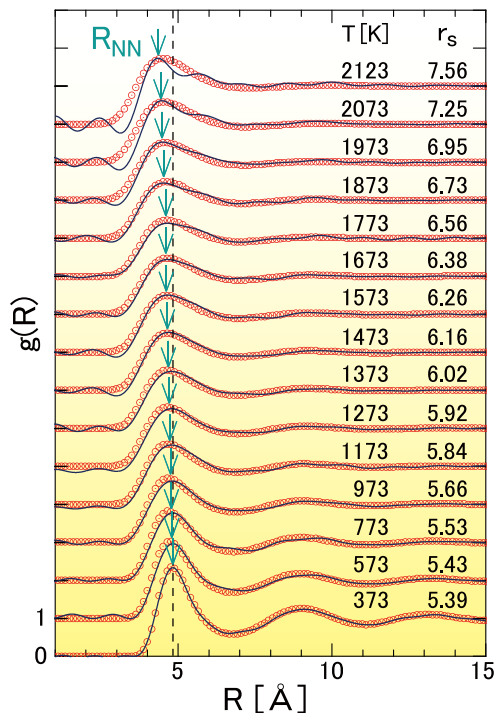

Fig. 1. Comparison between our theoretical results of the radial ion-ion distribution function $g(R)$ obtained by Monte-Carlo simulations on the model ionic system (the red open circle) and the experimental results by Matsuda *et al*. [Phys. Rev. Lett. **98**, 096401 (2007)] (the blue solid curves) for Rb. The distance between adjacent ions R_{NN}, which is determined by the first-peak position in $g(R)$, decreases with increasing r_s.
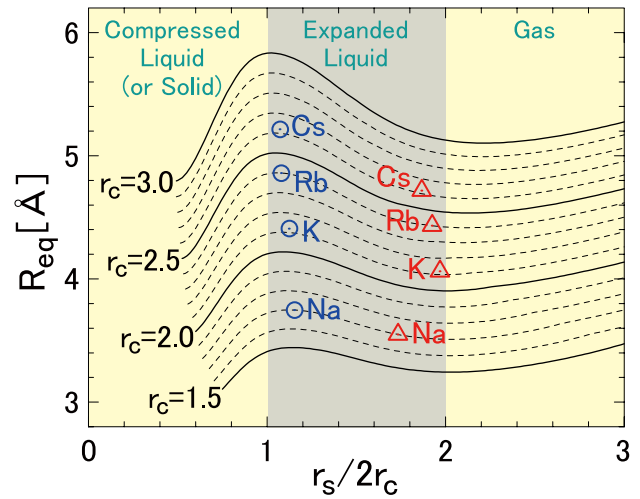

Fig. 2. Interionic equilibration distance R_{eq} with changing the ion-core radius r_c from 1.5 to 3.0 by 0.1 versus the ratio of r_s to $2r_c$. For each species, R_{eq} at n_{solid} is marked by a blue circle, while R_{eq} at $n_{critical}$ by a red triangle. R_{eq} decreases against the increase of r_s in the region of $1 < r_s/2r_c < 2$, roughly corresponding to the expanded-liquid regime.

only transport properties but also structural ones. This attraction is, in fact, a driving force for the liquid-gas phase transition necessarily accompanied by the metal-insulator transition [1].

Here we report on our recent study of the local ionic structure of an expanded liquid alkali metal on the basis of a model ionic system derived from the first-principles Hamiltonian by treating the electron-ion pseudopotential as perturbation [2]. Near the liquid-gas phase transition, we have found that R_{NN} the distance between adjacent ions *decreases* despite the increase of the mean interionic distance (or r_s the Wigner-Seitz radius) as shown in Fig. 1. This anomalous structural change is in sharp contrast with the normal one in solids and/or compressed liquid alkali metals near the liquid-solid phase transition, for which R_{NN} increases with increasing r_s.

In order to elucidate the physical origin of the local contraction of R_{NN}, we consider the interionic equilibration distance R_{eq}, which is determined by the minimum position in the effective interionic interaction potential, because R_{NN} coincides with R_{eq} for low n. From Fig. 2, it is found that R_{eq} *decreases* against the increase of r_s provided that the condition of $2r_c < r_s < 4r_c$ is satisfied with r_c being the radius of the ion core. By the careful analysis on the spatial dependence of the effective interionic interaction, we have revealed that this decrease of R_{eq} is attributed to an enhanced attraction working between valence electrons (or the strong tendency toward electronic phase separation caused by the XC effect), combined with the effect of excluding those electrons from the ion cores.

In Fig. 2, we have also indicated R_{eq} at n_{solid} (the solid densities at ambient pressure and temperature) and at $n_{critical}$ (the critical densities) for Na, K, Rb, and Cs. Since the density in the expanded liquid state is smaller than n_{solid} but larger than $n_{critical}$, we can conclude that the local contraction of R_{eq} and therefore R_{NN} is a universal phenomenon of an expanded liquid alkali metal.

References
[1] H. Maebashi and Y. Takada, J. Phys.: Condens. Matter **21**, 064205 (2009).
[2] H. Maebashi and Y. Takada, J. Phys. Soc. Jpn. **78**, 053706 (2009).

Authors
H. Maebashi and Y. Takada

Analytic Thermodynamics and Thermometry of Gaudin-Yang Fermi Gases

Oshikawa Group

Alkali fermionic atoms at tens of nanokelvins open a new arena of correlated quantum matter to be explored. Their interaction is tunable from attractive to repulsive infinity, by Feshbach resonance technique. This allows, for instance, the observation of universal properties of Fermi superfluids at unitarity. Recently, imbalanced populations of cold atoms in different hyperfine (spin) states is realized. In low dimensions, spin-imbalanced attractive Fermi gases exhibit very interesting phases. For example, in quasi-one-dimensional system, occurrence of Fulde-Ferrell-Larkin-Ovchinikov (FFLO) state is suggested.

Given the experimental developments, we have studied the thermodynamics of a one-dimensional attractive Fermi gas (Gaudin-Yang model) with spin imbalance. The exact Bethe Ansatz solution of this model has been known for decades. However, actual computation of physical quantities remained difficult, as it involves infinite number of coupled nonlinear integral equations.

We focused on the physically interesting regime of low temperature and strong coupling, and obtained a dramatically simplified set of algebraic equations governing the thermodynamics. It is then easy to numerically solve them to obtain temperature-dependent physical quantities with high precision. (See Fig. 1)

Moreover, the results on the thermodynamics give us insights into physics at finite temperature. The Gaudin-Yang Fermi gas at zero temperature exhibits three phases as the magnetic field is changed. At low fields BCS-type pairing occurs, while the spins are polarized at high fields. In the intermediate magnetic field regime, FFLO state is realized. Thus there are two quantum phase transitions induced by the magnetic field. At finite temperature, there are no longer sharp phase transitions in the one-dimensional system. Our study of the thermodynamics reveals several finite-temperature crossovers, which can be understood as quantum critical phenomena reflecting the quantum phase transitions at zero
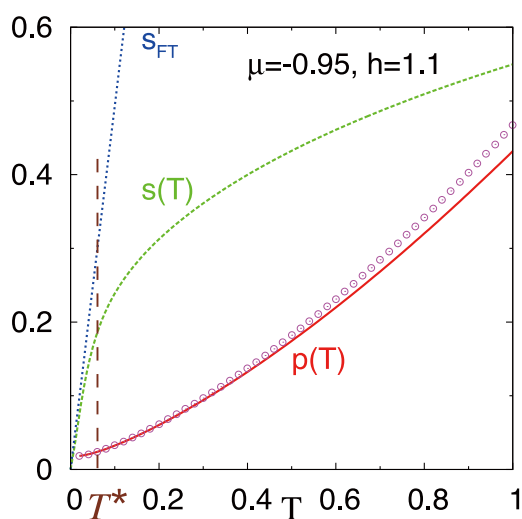

Fig. 2. (From Ref. [1]) Schematic finite-temperature "Phase diagram". The three phases at zero temperature correspond to distinct Tomonaga-Luttinger liquid phases. The crossover lines, which emerge from the quantum phase transition points, represent breakdown of the Tomonaga-Luttinger Liquid theory.

temperature. (See Fig. 2)

Finally, based on our results, we propose a method to determine the temperature of the spin-imbalanced one-dimensional Fermi gas accurately from experimentally obtained density profile. In fact, although the temperature is one of the most fundamental physical quantities, it has been difficult to estimate it in the experiment. This was primarily due to poor theoretical understanding of thermodynamics of the system. Our results can be used to help this crucial step in experimental studies.

References
[1] E. Zhao, X.-W. Guan, W. V. Liu, M. T. Batchelor, and M. Oshikawa, Phys. Rev. Lett. **103**, 140404 (2009).

Authors
E. Zhao[a], X.-W. Guan[b], W. V. Liu[a], M. T. Batchelor[b], and M. Oshikawa
[a]University of Pittsburgh
[b]Australian National University

Strong Coupling Superconductivity Mediated by Anharmonic Phonons in β-Pyrochlore Oxides AOs_2O_6 (A = K, Rb, or Cs)

Tsunetsugu Group

In recent years, much attention has been shown for the effects of local anharmonic ion oscillations in a cage structure on thermodynamics and transport phenomena in filled-skutterudites and β-pyrochlore compounds. They have a crystal structure of connected cages each of which contains one cation oscillating around its center. When the cage size is much larger than the radius of the contained cation, the oscillation of this ion is dramatically enhanced in its amplitude and thus becomes anharmonic. Indeed, anomalously large oscillation amplitudes are observed in these compounds. In β-pyrochlore oxides AOs_2O_6 (A = K, Rb, or Cs), A-cation is surrounded by an $Os_{12}O_{18}$ cage and its oscillation is found to be anharmonic particularly in KOs_2O_6, which can be understood by noting that the K-cation has the smallest size while the cage size is almost the same among the three members. Furthermore, high transition temperature of superconductivity is observed in KOs_2O_6 (T_c = 9.6 K) and T_c decreases with increasing cation size: 6.3 K for $RbOs_2O_6$ and 3.3 K

Fig. 1. (From Ref. [1]) Comparison of the temperature dependence of the pressure p obtained by numerically solving the full Thermodynamic Bethe Ansatz equations (circles), and that from our simplified set of equations (solid line). They show a good agreement especially at low temperatures. The entropy (green dashed line) is linear in temperature below the crossover temperature. The linear behavior at low temperatures agrees well with the Tomonaga-Luttinger liquid theory. The Tomonaga-Luttinger liquid theory breaks down above the crossover temperature.
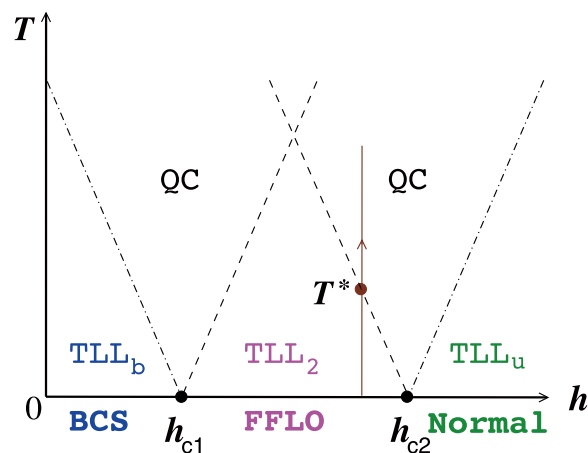
for CsOs$_2$O$_6$. This variation of T_c related to the cation size is expected to be due to the anharmonicity of ion oscillations.

Our group has recently performed a detailed quantitative analysis of the anharmonic A-cation oscillation and superconducting transition temperature in β-pyrochlore oxides [1]. We first examined local cation potential and then solved the three-dimensional Schrödinger equation for the cation quantum dynamics and calculated phonon propagator. It is important that the A-cation site has tetrahedral point group symmetry, and therefore the potential has a third order term, namely, a term proportional to *xyz*, where *x, y,* and *z* are the components of A-cation displacement from the equilibrium position. We chose the potential parameters so as to reproduce the experimental data of cation oscillation amplitude. Then, we applied the strong coupling theory of *s*-wave pairing combined with the obtained phonon propagator, and we calculated T_c for the three compounds.

Figure 1 shows the temperature dependence of cation oscillation amplitude $<x^2>$ for the three compounds compared with the experimental results. K-cation amplitude is much larger than Rb and Cs, and the temperature dependence differs even qualitatively; the curve is concave only for K. Our results well reproduce the experimental data, successfully capturing the genuine behavior. We also compared the temperature dependence of phonon density of states with the inelastic neutron scattering data, and confirmed the agreement. Thus, our phonon propagator is reliable to be used for calculating T_c.

The superconducting transition temperature T_c was calculated by setting the *same* electron-phonon coupling constant for the three compounds, including the additional contribution of higher-energy phonon observed in the neutron scattering experiments in order to make our calculation realistic. This additional contribution is determined from the calculation for the Cs-compound. The results are T_c = 10.5 K for K-, 5.7 K for Rb- and 3.4 K for Cs-compounds, respectively. These T_c values quantitatively agree with the experimental data and we find that the anharmonic phonons contribute up to 60 % of T_c for the K-compound, while much smaller for the other two.

To summarize, we have succeeded in the microscopic description of the anharmonic cation oscillations in β-pyrochlore compounds and reproduced the quantitatively
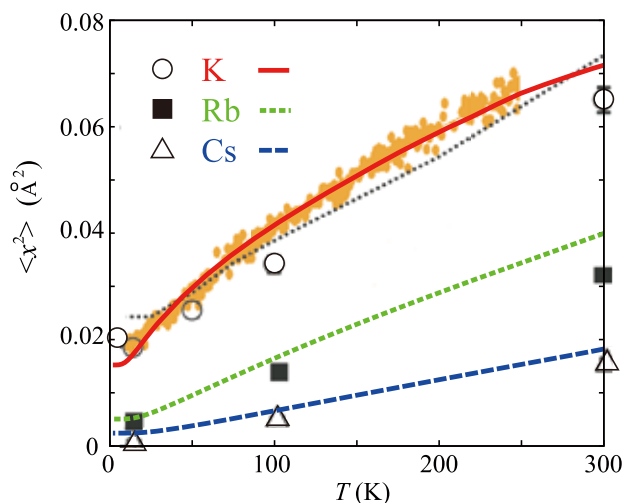

Fig. 1. Temperature dependence of cation oscillation amplitude $<x^2>$ for the β-pyrochlore compounds A = K (full line, red), Rb (dotted line, green) and Cs (dashed line, blue). The neutron scattering data are indicated by symbol ○ for K-, ■ for Rb- and △ for Cs-compounds, respectively. The black dotted line and the small orange dots show the x-ray scattering data and the recent neutron data for KOs$_2$O$_6$.

correct values of their superconducting transition temperature T_c. We have also demonstrated that the low-energy anharmonic phonon indeed enhances T_c. Recently, enhancement of T_c in high pressure was reported and it is important to examine the change in phonon anharmonicity in order to understand this interesting behavior. We hope our results shed a new light on the physics of superconductivity mediated by anharmonic phonons.

Reference
[1] K. Hattori and H. Tsunetsugu, Phys. Rev. B **81**, 134503 (2010).

Authors
K. Hattori and H. Tsunetsugu

Oxygen Reduction Reaction at Electrode-Solution Interface
−Reaction Mechanism vs Surface Property−

Sugino Group

Fuel cell reaction and water splitting are very familiar phenomena even for elementary school students, but even scientists feel difficulty in clearly explaining the whole process because it occurs so complicatedly at the solid-liquid interface. At the interface, the hydrated proton (H$^+$) and the electron (e$^-$), which are supplied from the solution and the electrode, respectively, are combined to form the hydrogen molecule (H$_2$) being catalyzed by platinum (Pt). Molecular level detail of this half cell reaction was previously described by our group using the first-principles molecular dynamics (FPMD) simulation, with the bias potential applied to a realistic water/Pt(111) interface model [1]. The other half of the cell, or the oxygen electrode, has been left unexplored by FPMD because of complexity of the reaction, although it is much more relevant to the recent fuel cell technology. In this context Okamoto (NEC), as a member of this group, did it systematically for noble metals (Pt, Pd, Ru, and Au) [2].

At the oxygen electrode, the oxygen molecule (O$_2$) is reduced step by step by four H$^+$ and e$^-$ to make two water molecules (H$_2$O). This process, or the oxygen reduction reaction (ORR), has been studied by many electronic structure calculations but these previous studies did it assuming the reaction pathways, and mostly took simply a surface model with water molecules neglected in the model. The present work [2] used the biased solid-liquid interface model to describe the four electron reduction step without assuming the pathways as did the previous work [1], and on the basis of the FPMD trajectory thus obtained, it explained why Pt better catalyzes ORR than Pd, Ru, and Au and why Pt is not the perfect catalysis.

The present simulation was done using the interface model as shown in Fig. 1 where one or two H$^+$ were introduced to mimic a biased acid solution. When the FPMD simulation was done for a few picoseconds, a H$^+$ came to the Pt surface and reduced O$_2$, which had been let adsorbed, to form OOH adsorbed on the surface. The O-O bond was then spontaneously broken to form two adsorbates O and OH, which were afterword reduced one by one by H$^+$ to form finally two H$_2$O. Such ORR pathways were found different for different surface and strongly dependent on the binding energies of the adsorbates. Ru, which binds O$_2$ more strongly, let O-O bond break immediately after the O$_2$
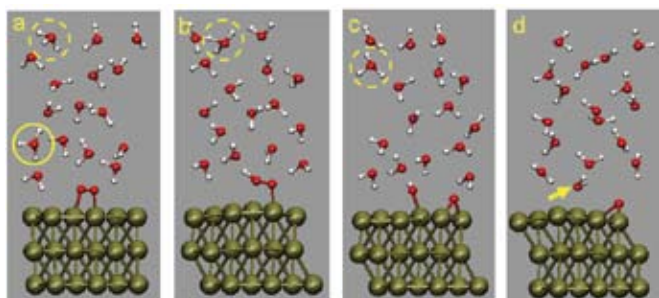
Fig. 1 (a-d). The Pt(111)-solution interface model used for the first-principles molecular dynamics simulation. The oxygen molecule adsorbed on the surface (shown with red spheres) is reduced step by step by the hydrated proton (shown with solid or broken circle) to make water molecule (shown with arrow in (d)). The pathways and mechanism of the four electron step for the oxygen reduction reaction were thus determined non-empirically.

adsorption (before the first reduction step), but Au, which binds it much weakly, did not let the bond break even after the second reduction step. The strong binding on Ru facilitates the reactant, O_2, from breaking the O-O bond, but hinders the products, O and OH, from leaving the surface thus leading to a lower catalytic activity. Opposite explanation can be used to explain low activity of Au. Pt and Pd have, in the meanwhile, a moderate binding energy and therefore show higher catalytic function.

Though Pt as well as Pd shows the best catalytic function among the noble metals studied, the activation energy for the reaction is not negligible so that a potential drop of about 0.4 V appears. Another model calculation shows that even the ideal voltage, 1.23 V, can be achieved, in principle, when binding energy of the reaction intermediates, O, OH, and OOH, can be optimized by using other (hitherto unknown) materials. It is a target of future calculation to find a surface of such ideal binding energy.

This way we have finally described the both electrodes using FPMD and demonstrated that the method is effective in explaining and predicting the electrocatalyzed interface reaction, which is too complicated to be properly understood without the help of simulation.

References
[1] M. Otani, I. Hamada, O. Sugino, Y. Morikawa, T. Ikeshoji, and Y. Okamoto, J. Phys. Soc. Jpn. **77** 024802 (2008).
[2] Y. Okamoto and O. Sugino, J. Phys. Chem. C **114**, 4473 (2010).

Authors
Y. Okamoto and O. Sugino

Dynamic Response of a Mesoscopic Capacitor

Kato Group

Dynamic control of electronic states in nanostructures has recently stimulated renewed interest since it is demanded in application to quantum information technologies. Toward rapid manipulation of electronic states, it is required to understand dynamic properties of coherent transport phenomena in nanoscale devices. It, however, is quite recent that it has been realized to measure GHz-frequency response of a nanostructure, which is called a mesoscopic capacitor [1] (a quantum dot coupled to a lead and a gate electrode, see the inset of Fig. 1). This system is described

by an effective RC circuit whose linear admittance takes the form $G(\omega) = (R_q - 1/i\omega C)^{-1}$. Experimentally, the resistive element R_q (called relaxation resistance) can be determined by the low-frequency expansion $G(\omega) = -i\omega C + \omega^2 C^2 R_q + O(\omega^3)$. In a classical circuit, Kirchhoff's law predicts that R_q should coincide with dc resistance R_{DC} at the point contact (QPC). Surprisingly, the relaxation resistance R_q takes a universal value $h/2e^2$ for single-mode transmission, which clearly differs from $R_{DC} = h/Te^2$ given by the Landauer formula with transmission probability T. This observation, indicating the breakdown of Kirchhoff's law, has been explained so far by the scattering theory proposed by Büttiker et al.[2] This theory, however, is based on the mean-field approximation, and is not justified in the presence of large charge fluctuation in the dot. Therefore, it remains an open question how electron correlation influences dynamic response of nanostructures.

We have studied the effect of Coulomb repulsion by considering a one-dimensional electron model [3,4]. We have examined dynamic resistance of the mesoscopic capacitor by combining perturbation theory, renormalization group arguments, and Monte Carlo calculation. The perturbation theory with respect to reflection at the quantum point contact proves that dynamic resistance takes a universal value $h/2Ke^2$ irrespective to reflection strength, where K is the Luttinger parameter. For intermediate and large reflection, however, drastic change in dynamic response has been found in the path-integral Monte Carlo calculation. We show the numerical result of the relaxation resistance on the charge-degenerate point at low temperatures in Fig. 1. One can see that for electron systems with no short-range repulsion ($K=1$) the relaxation resistance continues to take a universal value even for large reflection strength V at QPC. On the other hand, for electron systems with short-range repulsion ($K<1$), the relaxation resistance rapidly increases if V exceeds a critical value. This behavior reflects abrupt change in electron transport due to quantum phase transition. By renormalization group analysis, we have clarified that this phase transition belongs to the Kosterlitz-Thouless transition, and that phase-coherency of electrons completely loses beyond a critical value of V even at zero temperature.

Our result highlights the importance of electron correlation in transport through nanostructures, and is of much relevance to further development of dynamic manipulation in quantum dots. We note that drastic change of the relaxation resistance could be probed experimentally in quantum dots
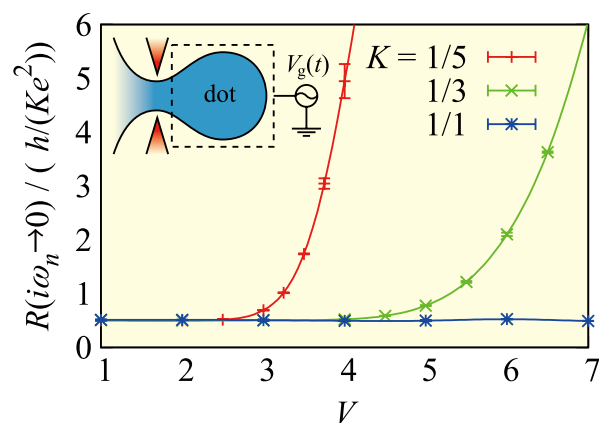

Fig. 1. Dynamic resistance as a function of reflection strength V at QPC. For $K=1$, it remains constant, while for $K<1$ it rapidly increases beyond a critical value of V. Inset, a schematic picture of the mesoscopic capacitor.

fabricated in an edge state in the fractional quantum Hall effect regime. Another experimental probe could also use one-dimensional quantum wires such as carbon nanotubes.

References
[1] J. Gabelli *et al*., Science **313**, 499 (2006)
[2] M. Büttiker, H. Thomas, and A. Prêtre, Phys. Lett. A **180**, 364 (1993).
[3] Y. Hamamoto, T. Jonckheere, T. Kato, and T. Martin, Phys. Rev. B **81**, 153305 (2010).
[4] Y. Hamamoto, Ph. D Thesis, The University of Tokyo (2010).

Authors
Y. Hamamoto[a], T. Jonckheere[b], T. Kato, and T. Martin[b]
[a]Institute of Physics, University of Ttsukuba
[b]Centre de Physique Théorique, Marseille, France

Temperature-Evolution of the Self-Consistent Screening of the Edge State around an Antidot

Iye Group

"Antidot" stands for a submicron area inaccessible to two-dimensional (2D) electrons. Typically, it is fabricated by etching away a small area of a GaAs/AlGaAs heterostructure. Figure 1 shows an AFM image of antidot array sample. Under a strong perpendicular magnetic field where the 2D electrons are in the quantum Hall regime, so-called edge states are formed around each antidot. Magnetoresistance exhibits oscillations due to the Aharonov-Bohm effect, as shown in Fig. 2. The oscillation period reflects change in the number of magnetic flux quanta enclosed by the circular edge state by one. It is determined by the Bohr-Sommerfeld quantization condition, $\pi r_m^2 B = m(h/e)$, where r_m is the radius of the circular edge state enclosing m flux quanta.

Figure 3 shows gray-scale plots of the oscillatory part of magnetoresistance as a function of magnetic field B and gate bias V_g at three different temperatures. The oscillation pattern shifts as the 2D electron density is varied by the gate
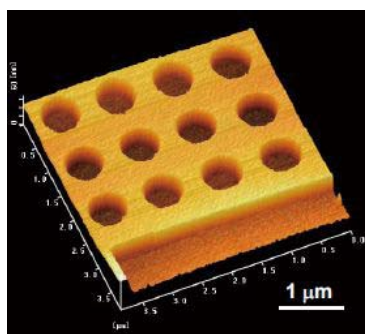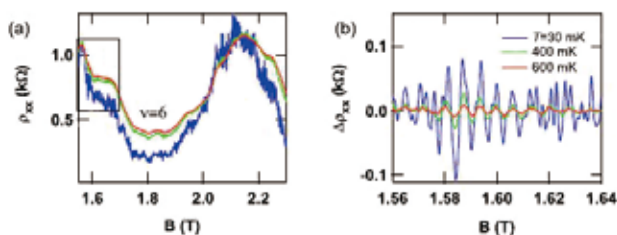

Fig. 1. AFM image of the antidot array sample.

Fig. 2. (a)Magnetoresistance of the antidot array sample around the ν=6 quantum Hall state. (b)Temperature dependence of the oscillatory part of resistance.
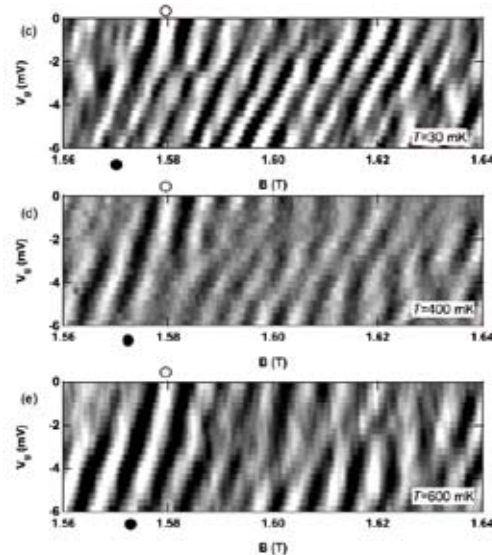

Fig. 3. Gray-scale plot (bright regions represent higher resistance) of the oscillatory part of magnetoresistance as a function of magnetic field B and gate bias V_g at three different temperatures. The slope of the stripe corresponds to the slope of the edge potential and its evolution with temperature furnishes information on the temperature dependent self-consistent screening.
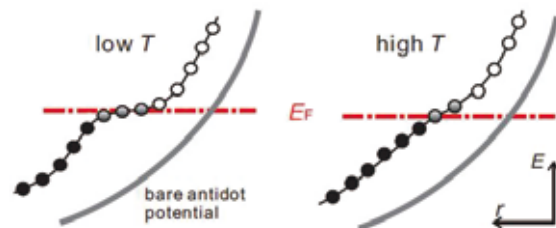

Fig. 4. Schematic drawings of the screened edge potential at low and high temperatures.

bias. The slope of the stripe in Fig.3 is given by the following relation,

$$\frac{\Delta V_g}{\Delta B} = -\frac{r_m}{2B}\left(\frac{\Delta r_m}{\Delta V_g}\right)^{-1} = -\frac{r_m}{2B}\left(\frac{dE}{dr}\right)_{r_m}\left(\frac{\Delta E_F}{\Delta V_g}\right)^{-1}.$$

The slope of the edge potential (dE/dr) differs significantly from the bare (unscreened) potential of the antidot edge, but is determined by self-consistent screening. It is seen that the slope of the stripe pattern in Fig.3 changes considerably with temperature, reflecting the reduction of screening effect with increasing temperature.

Reference
[1] M. Kato, A. Endo, S. Katsumoto, and Y. Iye, Phys. Rev. Lett. **102**, 086802 (2009).

Authors
M. Kato, A. Endo, S. Katsumoto, and Y. Iye

Pure Spin Current Injection into a Super-conducting Nb Wire

Otani Group

Recently, the ferromagnetic metal / superconductor hybrid structure is interested since the study on spintronic devices combined with superconductors may lead to the emergent technology in spintronics. Indeed, several

functional superconductive spintronic devices have been proposed theoretically. Spin relaxation phenomena in the superconductor have recently been reported [1], wherein spin currents were generated by direct spin polarized current injection from a ferromagnetic metal to a superconductor. The spin polarized current injection may induce the undesirable effects, such as a quench or suppression of the superconductivity due to heating, quasi-particle accumulations and so on. Thus, in the present work, we employed a non-local spin current injection, that is the indirect pure spin current injection into the superconductor in lateral multi-terminal structures. Moreover, both superconductor / normal metal / superconductor (SNS) junctions and lateral spin valves including superconducting wires are incorporated into the same lateral device to examine complementary the nature of superconductor / normal metal interfaces.

The fabrication process and a SEM image of a typical fabricated device are schematically shown in Fig. 1. The devices were fabricated by means of the electron-beam lithography followed by three angle shadow evaporation. The fabricated device consists of an SNS junction and a spin valve structure, which are framed as regions A and B in Fig. 1(b), respectively. In the spin valve structure, a Nb wire is connected to the Cu wire in between the two Py electrodes. Since the injection into the Nb wire via the transparent Nb/Cu interface results in the reduction of the measured spin signals [2], the difference of the pure spin current injection efficiencies between in normal and superconducting states may be estimated as the difference between the spin signals before and after the superconducting transition. On the other hand, the SNS junction carried supercurrent via the Nb/Cu interfaces once the Nb wire becomes superconductive. Since the supercurrent can flow without voltage drop even in the Cu wire, the superconductivity of the Nb/Cu interface can be investigated by measuring the resistance of the SNS junction.

The spin signals were measured with a probe configuration shown in Fig. 2(a) in representative temperatures 12 K and 370 mK for the normal and superconducting states, respectively. As shown in Fig. 2(b), the spin signals both in normal and superconductive state are 0.4 mΩ, which are clearly reduced compared with the spin signal of 1.2 mΩ for the reference spin valve without the inserted Nb wire. Since the spin signals measured in the samples without the inserted Nb wires are considered to reduce only slightly at low temperatures, no difference between the spin signals in the normal and superconducting states surprisingly means that the efficiency for pure spin current injection is preserved before and after the superconducting transition. Moreover, since the absorption phenomena of the pure spin current strongly depend on the interface properties, we examined the influence of the charge current to eliminate the possibility of a quench of the superconductivity at the Nb/Cu interfaces
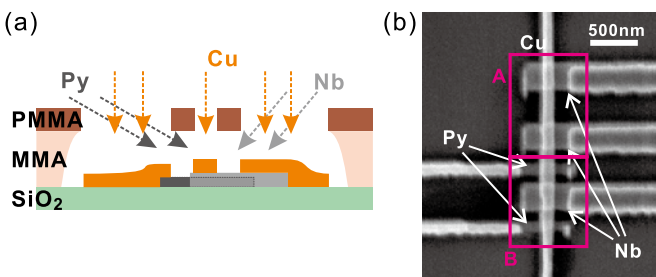

Fig. 1. (a) Schematic illustration of the fabrication procedure of a lateral hybrid structure by means of three angle shadow evaporation technique. (b) Scanning electron microscope (SEM) image of the fabricated device. The framed part A and B are an SNS junction and a spin valve structure with a Nb wire in between two Py wire, respectively.
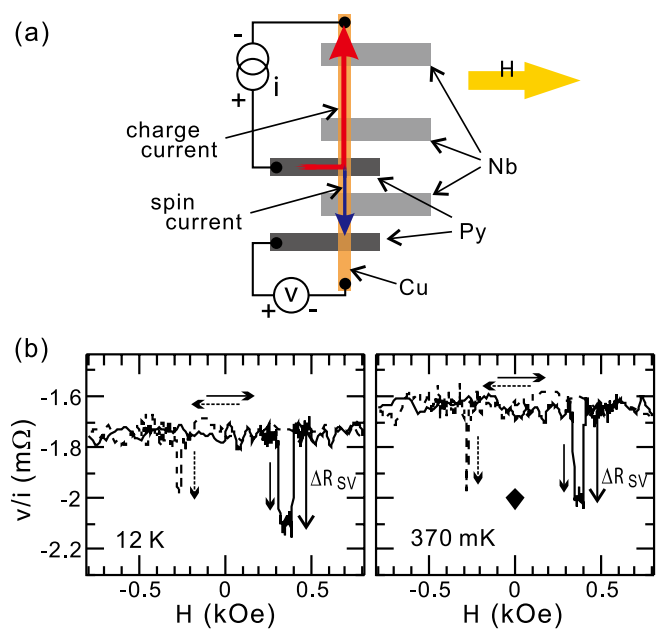

Fig. 2. (a) Schematic configuration of spin valve measurements. H shows an applied magnetic field. (b) Spin signals. Left and right plots are the results at 12 K and 370 mK, respectively. In the right plot, the black diamond indicates the non-local resistance in the anti-parallel state in the absence of the magnetic field.

under pure spin current injection with using the SNS junction incorporated in the same device. The results using the SNS junction show that the spin current absorption is not caused by a quench of the superconductivity of the Nb wire or the Nb/Cu interfaces.

We assume that more precise investigations and analyses such as temperature dependence and thickness dependence allow comparing with other experimental reports and revealing the mechanisms of the spin injection and diffusion in the superconducting state.

References
[1] N. Poli, J. P. Morten, M. Urech, A. Brataas, D. B. Haviland, and V. Korenivski, Phys. Rev. Lett. **100**, 136601 (2008).
[2] T. Kimura and Y. Otani, Phys. Rev. Lett. **99**, 196604 (2007).

Authors
Y. Otani, K. Ohnishi, T. Kimura[a]
[a]Kyushu University

Hole Injection Induces Local Motion of Surface Atoms through Electron-lattice Interaction

Komori Group

Strong excitation of local vibration can induce the motions of atoms and molecules in various materials. The most effective way to realize the highly excited vibration is to convert electronic excitation to vibrational one through the coupling between them. Moreover, the electronic excitation at extended states can realize a nonlocal manipulation of the atoms and molecules. At the clean Ge(001) surface, the carriers injected into the surface states reversibly and nonlocally alter the tilting orientation of the Ge dimers [1]. The change rate linearly depends on the tunneling current for both the electron and hole injections, indicating the single electron excitation process. Using scanning tunneling
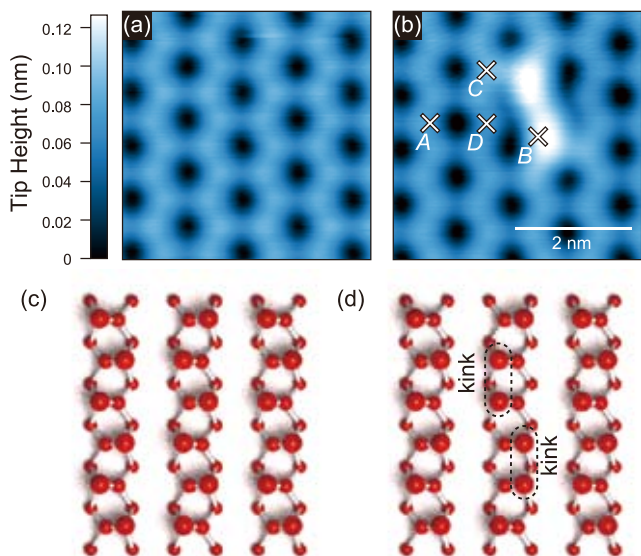
Fig. 1. Topographic STM images of the clean Ge(00l) surface at 80 K before (a) and after (b) creation of a kink pair by hole injection at the sample-bias voltage, $V_b = -0.7$ V. The corresponding ball models for the clean surface and the kink pair are given in (c) and (d). Large, middle, and small balls represent upper dimer, lower dimer and second layer Ge atoms. At $V_b = -0.5$ V, the kinks were stable, and imaged higher than the Ge dimers as in (b). The kink pairs are not always created in the dimer row including the tunneling point as schematically shown as the cross B, but in the neighboring dimer rows. The creation of the pair at the dimer row with the cross B can be detected as the change of the tunneling current at the crosses A, C and D.

microscopy (STM) and density functional theory, we have studied the microscopic processes of this nonlocal atom manipulation through the surface electronic excitation induced by hole injections [2].

Figure 1 shows STM images and models illustrating the change of the dimer tilting orientation. We can continuously monitor the local structure change as the tunneling current increase or decrease when the STM tip is fixed. Actually, the creation of the kink pair shown in Fig. 1(b) was detected at the positions above the points A-D as different values of the tunneling current. With increasing the excitation energy of the injected hole, the kink creation rate per electron first increases, once saturates, and then increases
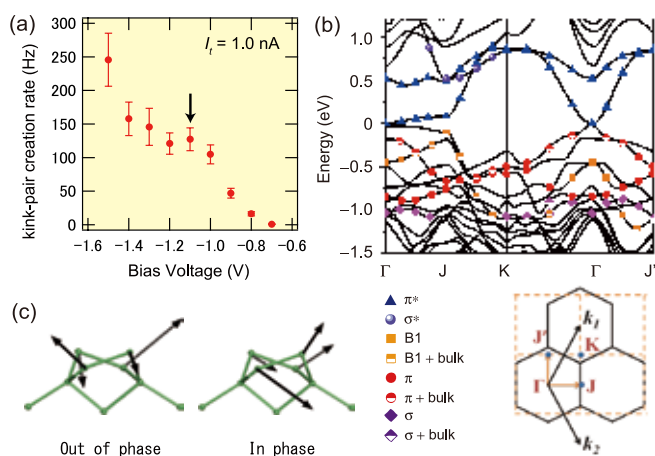

Fig. 2. (a) Kink pair creation rate as a function of the bias voltage during the hole injection. (b) Calculated band structure of the clean Ge(001) with the c(4×2) reconstruction. Band characters, the π*, π and σ states of the dimers, the dimer back-bond state (B1), and their mixing of the bulk states, are shown. Atomic structure of a slab model with 10 Ge layers was optimized. (c) Displacement vectors of the dimer atoms in the neighboring Ge dimers for two rocking modes, out of phase (left) and in phase (right). These two modes couple the surface electronic states.

again as shown in Fig. 2(a). The electronic states (Fig. 2(b)) and their coupling to two rocking modes of the adjacent dimer pair, out-of phase and in phase as illustrated in Fig. 2(c), were calculated for understanding the observed rate of the kink creation. The both modes strongly couple the unoccupied π*, occupied π and σ states of the dimers, and the occupied dimer back-bond states. The dimer orientation change is mainly induced by the carriers injected to the π* and π states. The observed two-step increase of the creation rate by the hole injection is attributed to the crossover of the electronic states from the π to σ. The hole injected to the B1 state induces the rocking mode vibration, but its energy is not enough to induce the change of the tilting orientation.

References
[1] K. Takagi *et al.*, Surf. Sci. **559**, 1 (2004).
[2] K. Tomatsu *et al.*, Phys. Rev. Lett. **103**, 266102 (2009).

Authors
K. Tomatsu, K. Nakatsuji, M. Yamada, B. Yan[a], C. Yam[a], Y. Xu[b], T. Frauenheim[a], W. Duan[b], and F. Komori
[a] Bremen University
[b] Tsinghua University

Elucidation of the Broadening Mechanism in the Softened C-H Stretching Mode of Cyclohexane on Rh(111)

Yoshinobu Group

As for the vibrational broadening of adsorbed species on single crystal surfaces, there are three line-broadening mechanisms; (i) inhomogeneity of adsorption sites (inhomogeneous broadening), (ii) the vibrational energy dissipation through excitation of e-h pairs or lattice phonons, and (iii) the vibrational phase relaxation (dephasing). In this study, the C-H stretching vibrations of cyclohexane on Rh(111) were investigated using infrared reflection absorption spectroscopy (IRAS) between 20 K and 89 K. Both normal and softened C-H stretching bands consisted of several sharp peaks at 20 K. With increasing the substrate temperature, the softened C-H stretching peaks became significantly broadened, but the normal C-H stretching peaks were little changed. The red-shift is caused by the local electronic interaction between the surface and axial C-H bonds (Fig. 1). Based on the temperature-dependent IRAS spectra, we conclude that the broadening is caused by the vibrational dephasing, where the softened C-H stretching mode is anhar-
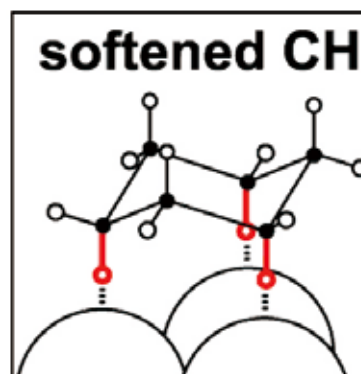

Fig. 1. A schematic of cyclohexane on a metal surface. The softened CH stretching mode is indicated in red.
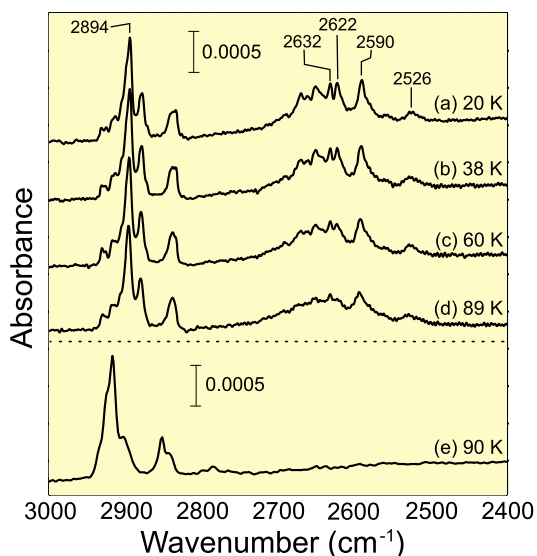
Fig. 2. (a) - (d) IRAS spectra of cyclohexane on Rh(111) at a near saturation coverage as a function of substrate temperature. (e) The IRAS spectrum of cyclohexane on H-saturated Rh(111) at 90 K.
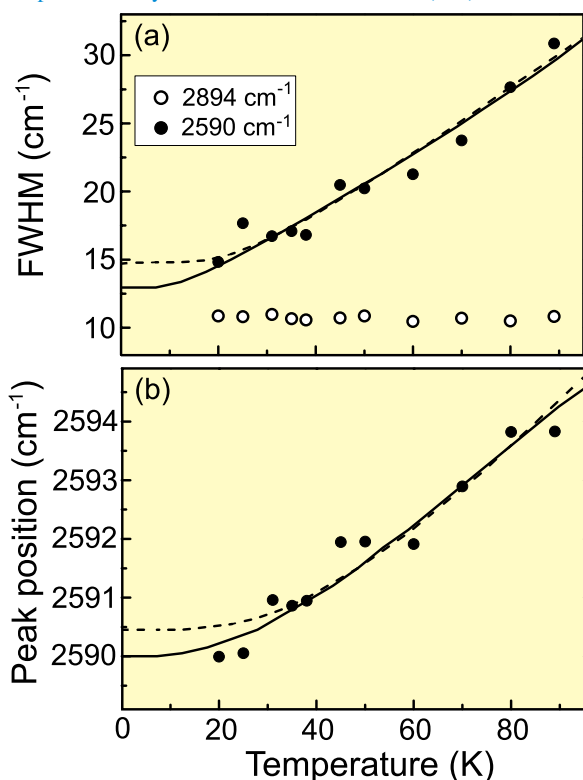

Fig. 3. (a) FWHMs and (b) peak positions of a softened C-H stretching peak at 2590 cm^{-1} (closed circles) as a function of temperature. FWHMs of a normal C-H peak at 2894 cm^{-1} are also shown (open circles). FWHMs and peak positions of the soft mode are fitted by the dephasing model. The details should be referred to the original paper [1].

monically coupled with a thermally excited low-frequency frustration mode.

Figure 2 shows a series of IRAS spectra of cyclohexane on Rh(111) at a submonolayer coverage as a function of substrate temperature. The C-H stretching bands were observed from 2400 cm^{-1} to 3000 cm^{-1}. The softened C-H stretching mode between 2800 cm^{-1} and 2400 cm^{-1} consisted of several sharp peaks at low temperature; with increasing temperature they became broad and overlapped each other. The observed multiple peaks indicate that cyclohexane molecules take several adsorption sites on Rh(111). In fact, we observed sharp low-energy electron diffraction spots indicating that cyclohexane molecules form an ordered, but

a higher-order commensurate phase on Rh(111). On the other hand, no soft mode was observed between 2700 cm^{-1} and 2500 cm^{-1} in the IRAS spectrum of cyclohexane on the H-saturated Rh(111) surface.

Figure 3 (a) shows the full-width at half maximum (FWHM) of the soft mode at 2590 cm^{-1}, and a width of a normal mode at 2894 cm^{-1} is also presented for comparison. The linewidth of the soft mode starts to increase about 40 K. On the other hand, the width of the normal mode is nearly constant over the observed temperature range. Fig. 2 (b) shows the peak position of the soft mode at 2590 cm^{-1} as a function of temperature. The peak at 2590 cm^{-1} as well as a small peak at 2526 cm^{-1} shift to higher wavenumber with increasing temperature.

The change of the soft modes at such low temperature region indicates that the temperature-dependent broadening of the individual softened C-H mode is triggered by thermal excitation of a low-energy frustrated mode of adsorbed cyclohexane; the dephasing plays an important role. Here we analyze the peak broadening and the peak shift of the softened C-H peak at 2590 cm^{-1} more quantitatively using the dephasing model proposed by Persson and Ryberg, and we conclude that a low-frequency mode coupled with the softened C-H stretching mode could be a frustrated translation parallel to the surface.

Reference
[1] T. Koitaya, A. Beniya, K. Mukai, S. Yoshimoto, and J. Yoshinobu, Phys. Rev. B **80** 193409 (2009).

Authors
T. Koitaya, A. Beniya, K. Mukai, S. Yoshimoto, and J. Yoshinobu

Spatial mapping of Ferromagnetic Resonance using a Radio-Frequency Probe

Hasegawa Group

Recent developments in microelectronic devices and spintronics lead researchers to the task of local characterization of the dynamical response in small magnetic structures and devices. Local measurement of ferromagnetic resonance (FMR), which can have quantized or localized modes due to sample boundaries, is one of the fascinating topics among them. Recently we have developed a radio-frequency (RF) probe with which one can locally excite FMR and detect its response. Using the probe, three kinds of FMR absorption signals were detected on a ferromagnetic disk, and spatial distribution of their intensity were imaged. These results demonstrate the potential of the local probe for spatially resolved FMR microscopy.

Figure 1(a) shows a schematic of our RF probe, an open-ended coaxial cable that transmits RF over 10 GHz with a sharp tungsten needle attached on its end. For the signal detection, the probe was located close to a sample in a typical distance of 0.1 mm. The RF current from the probe generates circular RF magnetic field in the sample, and its orthogonal component to static magnetic field H applied in the in-plane direction to the sample surface excites the magnetization. When the RF coincides with the FMR frequency, the resonance response appears as an absorption in the reflection spectrum (ΔS_{11}) measured with a vector network analyzer.
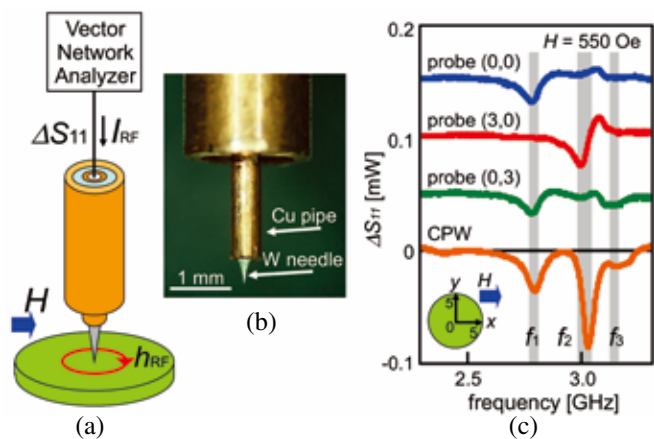
Fig. 1. Schematic of the RF probe and FMR signals detected on a YIG disk sample with the RF probe and a coplanar waveguide (CPW) located under the disk.

Figure 1(c) shows the absorption spectra taken by our RF probe at the three different positions on a polycrystalline Al-doped yttrium iron garnet (YIG) disk; one at the center of the disk, and the other two at the off-center sites. One can clearly recognize a resonance signal as an absorption dip at the frequency of f_1, f_2, and f_3, and notice whether the absorption signals are observed or not depends on the sites. The RF reflection spectrum we measured as a reference using a coplanar waveguide (CPW) located under the YIG sample, which detects FMR of its entire area, shows all the three signals, demonstrating the capability of the RF probe to locally detect the FMR signals.

By utilizing the scanning capability, we investigated the spatial dependence of the detected FMR signals, as shown in Fig. 2. Two-dimensional mapping of the absorption intensity for each signal clearly reveals node structure of each excited mode; no node for the f_1 mode, one node in the direction perpendicular (parallel) to H in the f_2 (f_3) modes. The spatial distribution and the frequency relation of the three modes lead us to identify f_1 and f_2 as magnetostatic backward volume wave (MSBVW) mode and f_3 as magnetostatic surface wave (MSSW) mode or the Damon–Eshbach (DE) mode excited in the sample.
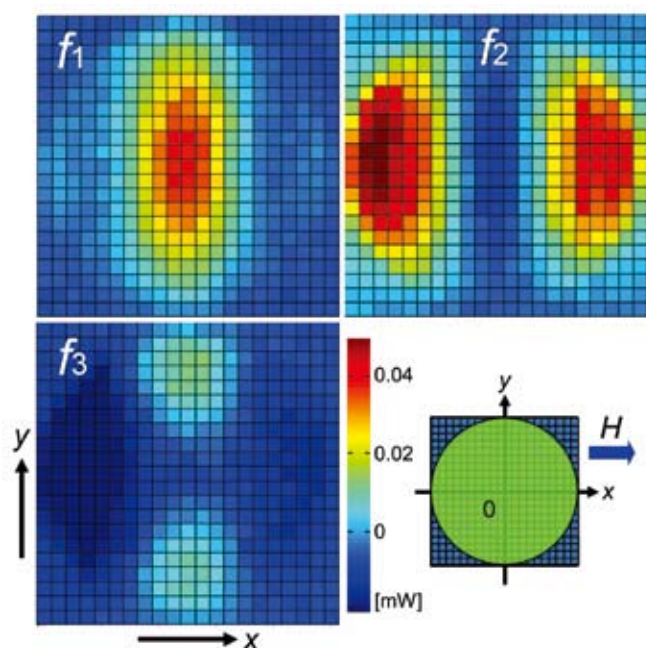

Fig. 2. Two dimensional mapping of the FMR signal intensities of the detected three modes; f_1, f_2, and f_3.

Although the spatial variation of the FMR detection is in millimeter range at the present moment, because of the sample size and the nature of the excited waves, the spatial resolution of the RF probe itself should be better. The spatial resolution for detecting FMR using an open-ended probe has been estimated to be an order of the tip curvature, which can be down to nanometer dimensions. We thus believe that this method will be a nanometer-scale imaging method of FMR, which is not accessible by the other techniques.

Reference
[1] Toshu An *et al.*, IEEE Magnetics Letters, **1** 3500104 (2010).

Authors
T. An[a], T. Eguchi, Y. Hasegawa, and P. Kabos[b]
[a]also PRESTO, Japan Science and Technology Agency
[b]National Institute of Standards and Technology, USA

Transport in LaTiO₃ / SrTiO₃ Heterostructures

Lippmaa Group

Interface layers of transition metal oxide heterostructures offer a new playground for studying ordering phenomena and carrier dynamics in low-dimensional systems. A particularly interesting case is the combination of $SrTiO_3$ with other insulating oxides, such as $LaAlO_3$ or $LaTiO_3$. It has been shown that such interfaces develop a two-dimensional high-mobility electron gas due to carriers that are accumulated in $SrTiO_3$ close to the interface. In our work, we focus on the transport properties of $LaTiO_3$ / $SrTiO_3$ interfaces, which are interesting because it is possible to combine a single unit cell layer of $LaTiO_3$ that has been predicted to show charge and spin ordering, with a 2-dimensional layer of high-mobility carriers in $SrTiO_3$. Due to the peculiar dielectric properties of $SrTiO_3$, it is also quite easy to modulate the density of carriers and the depth profile of carriers in the heterostructure by applying an external electric field on the heterostructure.
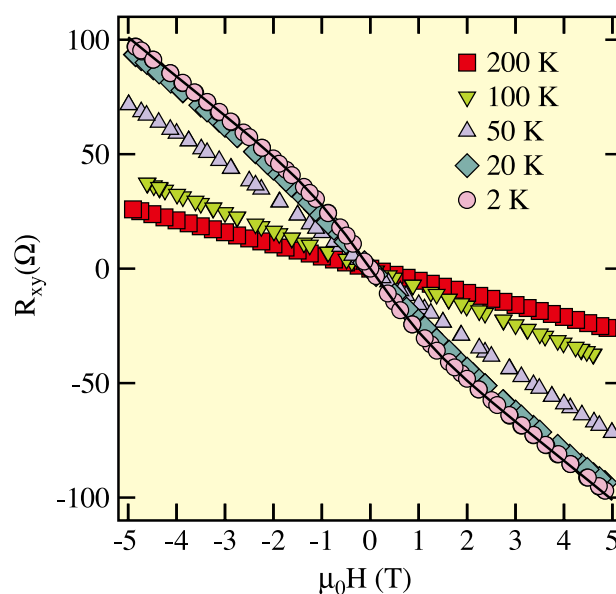

Fig. 1 Temperature dependence of Hall resistance for a single monolayer of $LaTiO_3$ embedded in $SrTiO_3$. A fit assuming two parallel conduction paths is shown for the 2 K data.
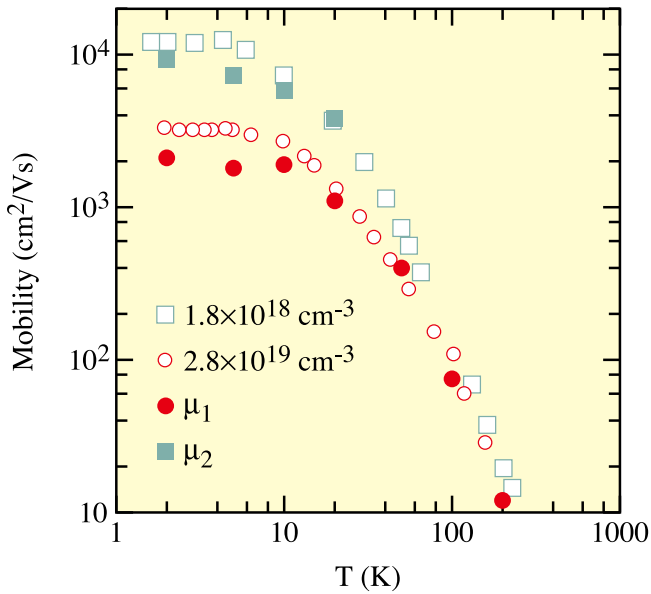
Fig. 2 Temperature dependence of mobilities of an interface layer (μ_1) and bulk layer (μ_2) for a single $LaTiO_3$ layer embedded in $SrTiO_3$, compared with the mobility behaviors of Nb-doped bulk $SrTiO_3$.

We grow the heterostructures by laser molecular beam epitaxy, which allows very accurate control over layer thicknesses. Typically a single monolayer of $LaTiO_3$ is grown on a $SrTiO_3$ substrate surface, and finally capped with a $SrTiO_3$ film. This produces a crystal where a single LaO atomic layer is embedded in a continuous $SrTiO_3$ perovskite lattice. Hall effect measurements are then used to measure the density, mobility, and spatial distribution of carriers, as shown in Fig. 1. At low temperatures, the Hall resistances are nonlinear, which can be understood in terms of multiple conducting layers in the heterostructures [1]. A fitting line for the 2 K data, assuming the presence of two conducting layers, is also shown in the plot. The multilayer Hall analysis allows us to extract the carrier densities and mobilities for a thin interface layer, which has a thickness of about 1 unit cell, and a thicker layer of electrons spread further into the $SrTiO_3$ substrate, to a depth of about 10 nm. Carrier mobilities reach 10^4 cm^2/Vs, with sheet densities in the 10^{13} cm^{-2} range.

Temperature dependence of carrier mobilities for the two layers, μ_1, corresponding to a thin interface layer and μ_2, which describes a thick layer of deep carriers in $SrTiO_3$, are shown in Fig. 2 and compared with the bulk mobilities of Nb-doped $SrTiO_3$ crystals. The temperature dependence shows that the carriers at the interface follow the bulk behavior and we can thus conclude that the conducting layers are indeed in the $SrTiO_3$ substrate. For the purpose of constructing truly 2-dimensional systems, it is necessary to eliminate the spread of carriers far into the $SrTiO_3$ substrate. This can be done, for example by field-effect, whereby the high-mobility carriers are depleted from the heterostructure by applying a large electric field, leaving only a very thin conducting layer in the first monolayer of the substrate. Such gated structures can be used to probe interface ordering phenomena.

Reference
[1] R. Ohtsuka, M. Matvejeff, K. Nishio, R. Takahashi, and M. Lippmaa, Appl. Phys. Lett. **96**, 192111 (2010).

Authors
R. Ohtsuka, M. Matvejeff, K. Nishio, R. Takahashi, and M. Lippmaa

Supersolid Density ρ_{SS} and the Critical Velocity V_c to Destroy the Supersolid State

Kubota Group

Supersolid (SS) state is a state characterized by having the lattice structure of a solid and simultaneous occurrence of superfluidity in this solid. The possibility for the Bose-Einstein Condensation (BEC) related phenomenon was noted in the late 1960's, supposing a finite density of zero point vacancies even as T approaches zero. Recent activities are ignited by the report on the possible non-classical rotational inertia ($NCRI$) observation in solid ^{4}He in 2004 [1]. Our detailed report [2] of the excitation velocity dependent torsional oscillator (TO) results indicate that the onset temperature T_o is rather high (~500 mK) and cannot be explained by BEC occurrence, but suggest the appearance of the vortex fluid (VF) state [3]. The observed period shift is caused by the non-linear rotational susceptibility ($NLRS$) of the VF state below T_o [3]. Independently, hcp solid ^{4}He was observed to show increased shear modulus at the same temperature range as the TO signal change [4]. Since then arguments not based on superfluids have gained strength. Namely, these arguments propose that some sort of glass transition may reproduce similar TO responses [5], or that dislocation motion is hindered by ^{3}He pinning at low temperatures and it becomes mobile at higher temperatures to explain the shear modulus change [4]. On the other hand it is becoming clear that TO response anomalies occur only in the hcp ^{4}He, but the shear modulus change is observed both for hcp ^{3}He and hcp ^{4}He [6].

Here we report our recent detailed study on the hysteretic behavior below 75 mK in the TO measurements and its detailed analysis [7]. We argue that a transition from the VF state to the SS state has been observed below
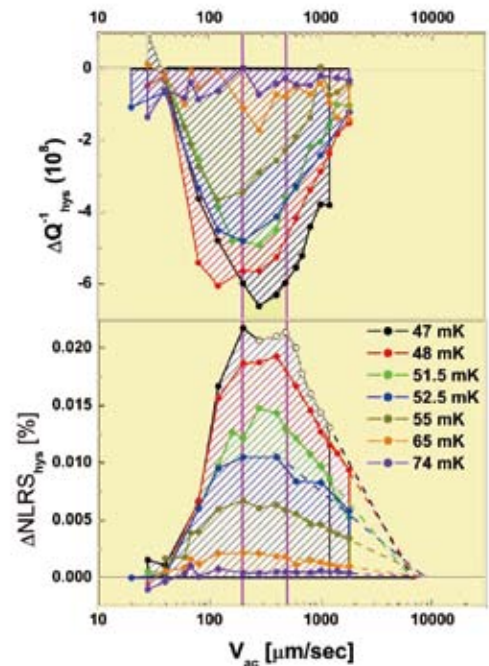

Fig. 1. "hysteretic" $\Delta NLRS_{hys} = NCRIF$ as well as ΔQ_{hys}^{-1} vs $logV_{ac}$. The hysteretic behavior starts at $V_{ac} \geqq 40\mu m/s$ at all $T's$ below ~75 mK. And both $\Delta NLRS_{hys}$ and ΔQ_{hys}^{-1} reach some extreme values for the range V_{ac}= 200 - 500$\mu m/s$. Then the absolute size of both quantities starts to decrease. We observe nearly $logV_{ac}$ linear decreases especially for $\Delta NLRS_{hys}$. From this linear extension of the $logV_{ac}$ dependence we obtain a critical velocity, 6~10 mm/s to suppress the $NCRIF$=ρ_{ss} to zero, which compares well with $V_c = h/(m^4 \xi_0 \pi)$ = ~ 6 -12 mm/s, for $\xi_0 = 50$ - 25 nm. See text.

T_c ~75 mK. It is characterized by the hysteretic behavior and the critical velocity V_c of ~ 1 cm/s to destroy the SS state [7]. We propose that the maximum of the nonlinear rotational susceptibility change across a systematic hysteretic loop to be the supersolid density ρ_{ss} at a temperature T. We could construct ρ_{ss} as a function of T in absolute units, namely in kg/m^3. From this absolute supersolid density we could evaluate a characteristic coherence length, Josephson's length, ξ by the following formula[8]: $\xi = m^2 k_B T/\{(h/2\pi)^2 \rho_{ss}\}$, where $h/(2\pi)$ and k_B are Planck's and Boltzmann's constants. Figure 1 shows the hysteretic component of the TO response as a function of the excitation velocity V_{ac} from a 49 bar hcp ^{4}He sample in a cylinder of 10 mm diameter and 4 mm high [7]. The hysteretic component appears both in the *NLRS* and the energy dissipation ΔQ^{-1} above V_{ac} ~ 40 μm/s and they reach maximum deviation around V_{ac} =200 μm/s and then stay almost constant at a constant T until V_{ac} ~500 μm/s. We find that the hysteretic component $\Delta NLRS_{hys}$ decreases linearly with $logV_{ac}$ above ~ 500 μm/s. We had reported a similar $logV_{ac}$ linear decrease of the *NLRS* signal for the VF state, but with orders of magnitude smaller V_{ac} values. This dependence was first discussed for solid He as evidence of involvement of quantized vortex lines penetrating the sample by P. W. Anderson [3] as well as by Kubota group [2,9]. With an extension of the above $logV_{ac}$ linear dependence for the hysteretic component we observe that the hysteretic component $\Delta NLRS_{hys}$ is suppressed to zero at ~ 1 cm/s for the lowest temperatures. We can claim this velocity to be the critical velocity V_c to destroy the SS state. Using the proposed ρ_{ss} and obtained coherence length ξ (see Fig. 2), one can evaluate this critical velocity at $T = 0$ K : $V_c= h/(m^4 \xi_0 \pi) =$ ~ 6-12 mm/s. This is rather surprising agreement and supports our proposal of the supersolid density ρ_{ss}.

Figure 2 shows the critical behavior of the evaluated ξ vs reduced temperature with T_c = 56.7 mK. From this plot we could estimate the ξ extrapolated to $T = 0$K, ξ_0, which can be regarded as the vortex core diameter a_0 and could give an independent estimate of the critical velocity as discussed above.

We surely observed the transition from the VF state into the SS state, which is characterized by the critical velocity, V_c ~ 1 cm/s, consistent with our evaluation of the supersolid density ρ_{ss}. Our results, Ref. 9 together with Ref. 7 also indicate coexistence of the VF state and the SS state over a temperature range 30 mK < T < 75 mK, which suggests a
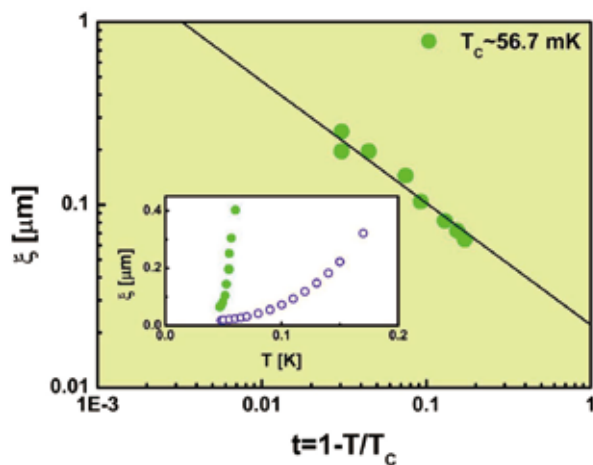

Fig. 2. Critical behavior of ξ obtained from the T dependent $\Delta NLRS_{hys}$ =ρ_{ss} data at 200 μm/s in Fig. 1. We took T_c = 56.7 mK, supposing ρ_{ss}= $(1-T/T_c)^\gamma$= t^γ with γ=2/3. We obtain ξ_0 ~ 25 to 50 nm by simple extrapolations, horizontal and straight extension of the linear relation. Inset shows ξ for the SS state ξ_{SS} as well as for the VF state ξ_{VF} in linear scales. $\xi_{SS} > \xi_{VF}$ at all T where they coexist.

first order transition. With the critical behavior as expressed in Fig. 2 it may well be the first clear manifestation of the "weak first order transition", other than one in liquid crystals, first discussed phase by B. I. Halperin *et al.*,[10].

References
[1] E. Kim and M. H. W. Chan, Nature **427**, 225 (2004); Science **305**, 1941 (2004).
[2] A. Penzev, Y. Yasuta, and M. Kubota, Phys. Rev. Lett. **101**, 065301 (2008).
[3] P. W. Anderson, Nature Physics **3**, 160 (2007).
[4] J. Day and J. Beamish, Nature **450**, 853, (2007).
[5] B. Hunt *et al.*, Science **324**, 632 (2009).
[6] J. West et al., Nature Physics **5**, 598 (2009).
[7] M. Kubota, N. Shimizu, Y. Yasuta, P. Gumann, and S. Nemirovskii, J. Low Temp. Phys. **158**, 572 (2010); N. Shimizu, Y. Yasuta, and M. Kubota, arXiv:0903.1326.
[8] N. P. Mikhin, V. E. Syvokon, T. Obata and M. Kubota, Physica B **329- 333**, 272 (2003); M. E. Fisher, M. N. Barber, and D. Jasnow, Phys. Rev. A **8** No.2, 1111 (1973).
[9] S. Nemirovskii, N. Shimizu, Y. Yasuta, and M. Kubota, arXiv: 0907.0330.
[10] B.I. Halperin, T. C. Lubensky, and Shang-keng Ma, Phys. Rev. Lett. **32**, 292 (1974).

Authors
N. Shimizu, Y. Yasuta, S. Nemirovskii[a], and M. Kubota
[a]ISSP visiting Professor(Sept-Dec. 2008); Inst. Thermophysics, RAS, Novosibirsk, Russia.

Magnetotransport of Dirac Fermions: Graphene and Organic Conductors

Osada Group

Magnetotransport features of massless Dirac fermions have been studied in two low-dimensional systems; graphene and layered organic conductors.

One of the most remarkable phenomena observed in graphene is the half-integer quantum Hall effect (Fig. 1(a)). It originates from the nature of two-dimensional (2D) massless Dirac fermions. In Hall-bar-type devices, transport features of quantum Hall state are well described by the edge channel picture by Landauer and Buttiker. In order to study edge channels in graphene as a bipolar quantum Hall system, we have performed magnetotransport measurements in the graphene FET device with the additional top gate electrode that controls local carrier density. Samples have been prepared using mechanical exfoliation and electron-beam lithography technique. The Hall resistance across the top-gated region is fractionally quantized as expected by the Landauer-Buttiker picture (Fig. 1(b)). By reversing magnetic field orientation, we have observed the breaking of electron-hole symmetry of edge channel transport in graphene.

Recently, it has been pointed out that several organic conductors, α-(BEDT-TTF)$_2$I$_3$, α-(BEDT-STF)$_2$I$_3$, etc. are multilayer Dirac fermion systems, which consist of parallel stacked conducting layers. The electron system of each layer is a 2D massless Dirac fermion system with in-plane anisotropy, and the Fermi level is located at the Dirac point resulting in zero-gap structure. On the other hand, unusual magnetotransport behaviors have been reported in these compounds; saturation of in-plane resistance (ρ_{xx}), local maxima of in-plane Hall resistance (ρ_{yx}), negative interlayer magnetoresistance (ρ_{zz}), and anomalous angle-dependence of interlayer Hall resistance (ρ_{zx}) obeying the "cotθ-law". The origins of these phenomena have been open questions for a long time. Based on the multilayer Dirac fermion model, we
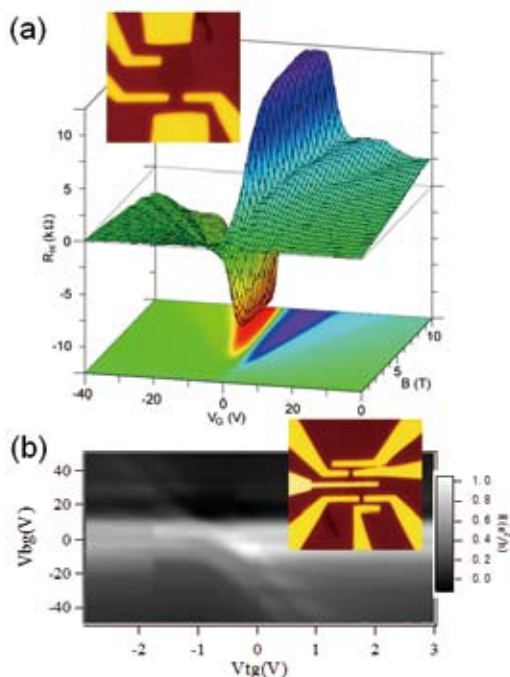
Fig. 1. (a) Half-integer quantum Hall effect in graphene. Inset: Microscope image of graphene FET device. (b) Top- and back-gate voltage dependence of Hall resistance across the top-gated region. Inset: top-gated graphene FET device.

have theoretically reconsidered the mysterious magnetotransport features. We consider the quantum limit where only the $n=0$ Landau level exists at the Fermi level. In the massless Dirac fermion system with the Fermi level located at the Dirac point, the quantum limit is easily reached even in low magnetic fields. We employ the perturbation method called the "tunneling picture", which treats interlayer coupling as a perturbation. The conductivity is expanded into a power series of the interlayer transfer energy t_c. At the limit of weak interlayer coupling, the lowest order term of t_c gives the dominant contribution to the conductivity. We have evaluated the lowest order term for all elements of conductivity tensor. By calculating the inverse tensor of conductivity, we have successfully obtained the approximate formulae of all elements of resistivity tensor. They reproduce all of the observed behaviors qualitatively, particularly, negative interlayer magnetoresistance $\rho_{zz} \sim 1/|B_z|$ and anomalous angle-dependence of interlayer Hall resistance $\rho_{zx} \sim |B_y/B_z| = \cot\theta$. They are characteristic phenomena in multilayer Dirac fermion systems at the quantum limit. The present result strongly suggests that massless Dirac fermions really exist in several organic conductors.
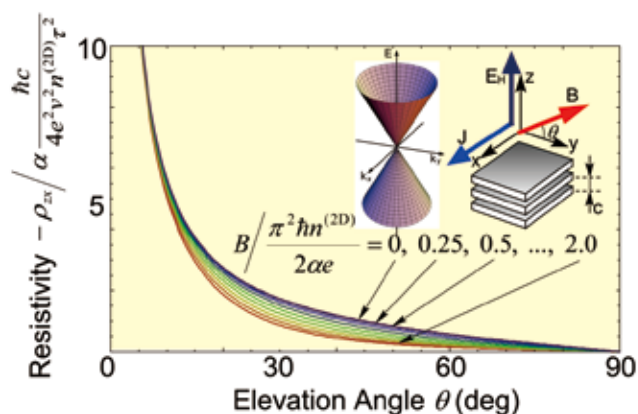

Fig. 2. Interlayer Hall resistivity ρ_{zx} calculated assuming multilayer Dirac fermion system with incoherent interlayer coupling.

Authors
T. Osada, D. Nakahara, H. Okunaga, A. Tsukuda, K. Uchida, and T. Konoike

Pressure-Induced Ferromagnetic to Antiferromagnetic Phase Transition in Ce₂Ni₅C₃

Uwatoko Group

The cerium transition-metal carbide $Ce_2Ni_5C_3$ crystallizes in the tetragonal $La_2Ni_5C_3$-type structure with a ferromagnetic phase at the T_C = 2.3 K at ambient pressure. According to the specific heat data, an obvious λ-type anomaly and a shoulder-type anomaly were observed around T_C. $Ce_2Ni_5C_3$ also has the Shastry Sutherland lattice structure, which will be described in the inset of Fig. 2. Therefore, the broad anomaly of the specific heat in $Ce_2Ni_5C_3$ just above T_C may come from the same origin, although $Ce_2Ni_5C_3$ eventually orders ferromagnetically.

In order to detect the magnetic anomaly, we performed ac magnetic susceptibility measurements, which are highly sensitive to a ferromagnetic transition. We report the results of temperature dependence under pressure and magnetic field of the ac magnetic susceptibility of $Ce_2Ni_5C_3$ using a newly developed palm cubic anvil cell (PCAC). The PCAC was designed as a self-clamp-type cell, in order to extend the temperature range to lower temperatures down to 0.5 K as shown in Fig 1.

The temperature dependence of ac magnetic susceptibility $\chi'(T)$ have been measured under pressure. At 0.9 GPa, $\chi'(T)$ has a peak at T_C ~ 2 K corresponding to the ferromagnetic ordering temperature. We found that a new anomaly appears at T^* ~ 1.7 K at 3.6 GPa. In contrast to the pressure dependence of T_C, T^* shifts to higher temperatures with increasing pressure. In order to characterize these ordered states, we measured the ac magnetic susceptibility $\chi'(T)$ at different frequencies under several typical pressures. Clear frequency dependence is observed below T_C at 0.9 GPa. Such behavior can be observed in ferromagnetic compounds due to the dynamics of magnetic domain walls. At 3.6 GPa, the $\chi'(T)$ curve exhibits a double-peak structure. Whereas T_C
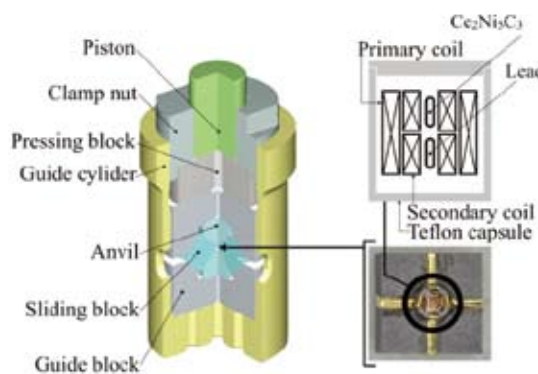

Fig. 1 . (a) A schematic drawing of the Palm cubic anvil cell. It consists of six tungsten carbide anvils, and a cube-shaped pressure medium made of pyrophyllite is compressed from three directions to achieve hydrostatic pressure. (b) The arrangement of the coils for ac magnetic susceptibility measurements, together with a photograph of the cubic gasket. The $Ce_2Ni_5C_3$ and the lead were shaped into plates and placed inside the pickup coils. The ac magnetic susceptibility was measured with a modulation magnetic field of 2 Oe at frequencies f = 11, 101, 307, and 1017 Hz.

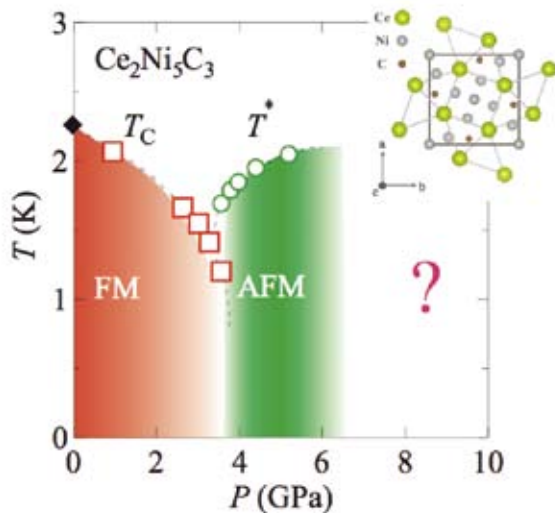Fig. 2. Pressure-temperature phase diagram of $Ce_2Ni_5C_3$. The crystal structure of $Ce_2Ni_5C_3$ consists of alternating layers of Ce-Ni and Ni-C planes stacked along the c-axis (see inset). The right-hand side figure displays the schematic representation of the network of Ce atoms in the ab-plane. The Ce ions form a combination of squares and isosceles triangles. This network of Ce ions is topologically equivalent to the Shastry-Sutherland lattice structure. Squares and circles represent the ferromagnetic and antiferromagnetic transition temperatures, respectively. The ferromagnetic transition temperature at ambient pressure indicated with the diamond is determined from the specific heat data.

shifts toward higher temperatures with increasing frequency, T^* is almost frequency independent. At 5.2 GPa, we no longer observe the frequency-dependent anomaly associated with T_C, while the peak at T^* still survives. Also, we measured $\chi'(T)$ at dc fields of 0, 700, and 1000 Oe to investigate the magnetic field response of the T^* anomaly. The transition temperature moves toward lower temperatures with increasing applied magnetic field, suggesting that the magnetic transition at T^* is due to the antiferromagnetic ordering of Ce moments.

In Fig. 2, we summarize the anomalies obtained from ac magnetic susceptibility measurements at the frequency f = 307 Hz to construct a P-T phase diagram. The ferromagnetic transition temperature T_C decreases with increasing pressure, and an extrapolation suggests a critical pressure $P_C \sim 3.8$ GPa. The ferromagnetic phase becomes unstable above 3.0 GPa, and the antiferromagnetic phase appears above T_C. At 3.6 GPa; successive magnetic phase transitions are observed at 1.7 K and 1.2 K. The antiferromagnetic phase is stabilized by pressure, and the temperature T^* develops in this pressure region. Similar switching behavior from ferromagnetism to antiferromagnetism is observed in ferromagnetic Ce-based intermetallic compounds, such as $CeAgSb_2$. The isostructural compounds $R_2Ni_5C_3$ (R = Sm, Gd), which have a smaller unit cell volume than $Ce_2Ni_5C_3$ due to lanthanide contraction, show antiferromagnetic ordering. Therefore, the change of magnetic phase from ferromagnetism to antiferromagnetism could be interpreted as the sign change in the RKKY interaction. These compounds are situated at the border line between ferromagnetic and antiferromagnetic ordering, and thus tuning of the lattice parameters by applying pressure can change the magnetic structure. This feature is expected to originate from short-range ordering due to competing antiferromagnetic and ferromagnetic interactions. $Ce_2Ni_5C_3$ might potentially possess a magnetic instability at ambient pressure.

Reference
[1] A. Yamada *et al*., Solid State Comm. **150** 725 (2010).

Authors
A. Yamada[a], K. Matsubayashi, Y. Uwatoko, K. Kondo[a], S. Katano[a], and M. Kosaka[a]
[a]Saitama University

Observation of Wave-packet Splitting and Quantum Interference with Femtosecond Resolution

Suemoto Group

Real time observation and control of the nuclear wave-packet (WP) are major subjects in photo-chemistry and physics. In the condensed matter systems, WP dynamics is particularly interesting, because it reflects the collective motion of atoms during generation and annihilation of the localized elementary excitations and creation of photoinduced phases.

We have been studying the one-dimensional halogen-bridged Pt complex, which has the charge density wave (CDW) in the ground state and various excited states, i.e., self-trapped excitons (STE), polarons, spin-solitons (SS) and charged-solitons (CS). Figure 1 (a) is the 2-D plot of the time-evolution of the luminescence spectrum at 4 K, which reflects the squared amplitude of the nuclear wavefunction. In the energy region above 0.4 eV, oscillation of the WP around the minimum of the adiabatic potential energy surface (see Fig. 1 (b)) is seen. In this "STE region", several cycles of damped oscillation with a period of about 300 femtoseconds (fs) are clearly observed. This result is consistent with our previous work [1]. The new finding is seen in the lower energy region. In Fig. 1 (a), we can recognize some
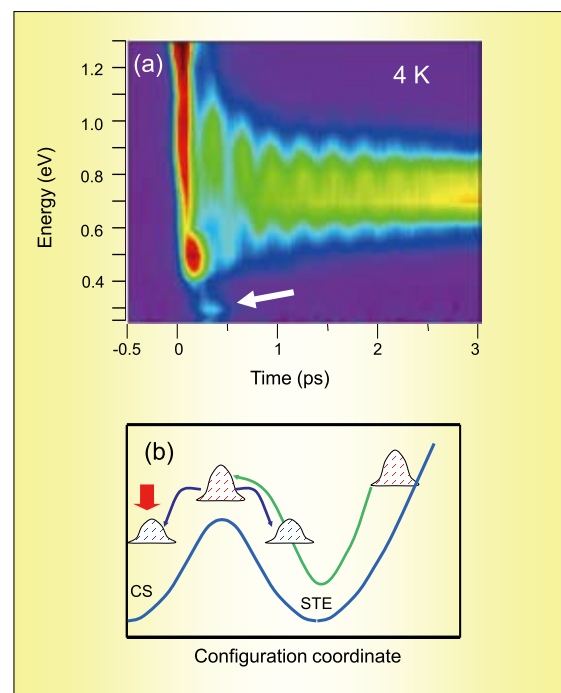

Fig. 1. (a) Color mapping of time-resolved luminescence spectra in quasi-one-dimensional Br-bridged Pt complex measured with the up-conversion technique. The "split-off component" is indicated by a white arrow. (b) A double-well potential representing the STE state and soliton-pair state. The wave-packet starts propagating from the right and splits into two parts on top of the barrier.
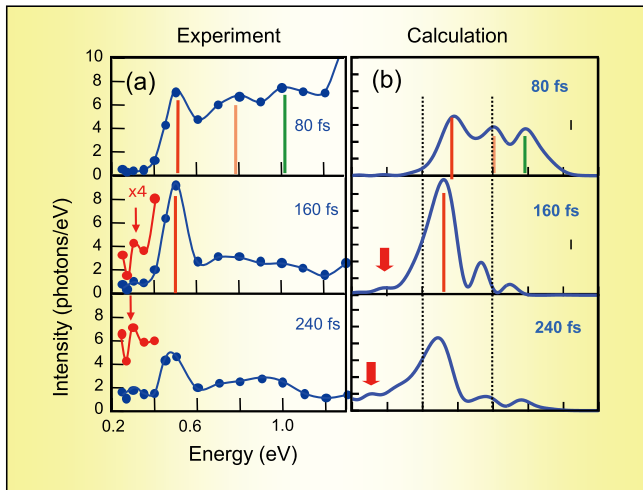
Fig. 2. (a) Time-resolved luminescence spectra at 80, 160 and 240 fs. The split component appears on the left (red arrows). (b) Calculated squared amplitude of the wavefunctions at 80, 160 and 240 fs. The vertical dotted lines indicate the positions of potential minimum and maximum. Colored vertical bars indicate the quantum interference peaks.

component splitting off from WP of STE with a slight tilt angle to the right in the first swing of the vibration below 0.4 eV beyond the turning point of WP (indicated by a white arrow). This component can be assigned to a split WP (indicated by a red arrow in Fig. 1 (b)), as discussed below.

The details can be seen more clearly in the time-resolved spectra in Fig. 2 (a). The WP started from the right spreads around the potential minimum (around 0.8 eV) at 80 fs and it reaches the left turning point at 160 fs, showing a pronounced peak at 0.5 eV. The peak diminishes and the split component at 0.3 eV grows up at 240 fs. The time-developing wavefunctions are calculated based on a double-well potential (see Fig. 1(b)), which mimics the STE state (right) and the soliton-pair state (left) separated by a potential barrier. The results (Fig. 2 (b)) are in good agreement with the experimental results. The split-off components (indicated by downward red arrows) are seen both in (a) and (b). In addition, ripple structures appear at 80 fs as a result of interference of the wavefunctions involved in WP. By counting the number of ripples, we can directly know the most significant vibrational quanta representing WP.

In conclusion, we successfully observed, for the first time, the generation process of a metastable state as a splitting of a wave-packet representing the lattice rearrangement in solid.

References
[1] T. Matsuoka, J. Takeda, S. Kurita, and T. Suemoto, Phys. Rev. Lett. **91**, 247402 (2003)
[2] Y. Takahashi, K. Yasukawa, S. Kurita, and T. Suemoto, Phys. Rev. B **81**, 081102 R (2010)

Authors
Y. Takahashi, K. Yasukawa, S. Kurita[a] and T. Suemoto
[a] Yokohama National University

Thermal-Equilibrium Relation in Optical Spectra of Semiconductor Quantum Well
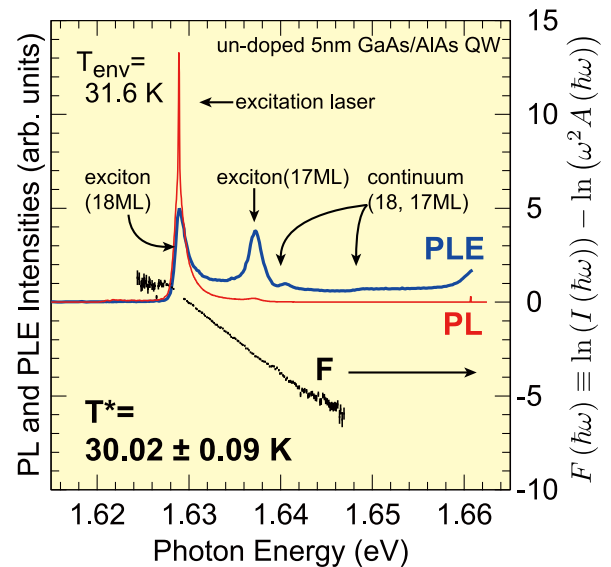
Akiyama Group

Fig. 1. PL (red curves) and PLE (blue curves) spectra from an un-doped 5 nm GaAs/AlAs QW. PL spectra are obtained under resonant excitation. Black dots with error bars indicate the value of function F deduced from PL and PLE spectra. Temperature $T^* = 30.02$ K, which are calculated from the slope of function F, shows excellent agreement with environment temperature $T_{env} = 31.6$ K measured with a Si diode thermometer.

Kennard-Stepanov (KS) relation is a fundamental thermal-equilibrium relation between optical spectra of emission (I) and absorption (A) [1,2]. Using this relation for photoluminescence (PL) and PL-excitation (PLE) spectra, we have investigated the energy distribution of carriers in doped [1] and un-doped semiconductor quantum wells (QW) fabricated by molecular beam epitaxy. Through improving sample homogeneity as well as S/N ratio of measured spectra, we revealed that temperature T^* deduced from optical spectra shows agreement (deviation) with environment lattice temperature T_{env} under resonant (non-resonant) excitation condition, which indicates the formation of quasi-(non-) equilibrium carrier distribution in both doped and un-doped QWs.

PL and PLE spectra of an un-doped 5 nm GaAs/AlAs single QW at $T_{env} = 31.6$ K are shown in Fig. 1. The red and blue curves indicate PL and PLE spectra, respectively. High homogeneity of QW is reflected in exciton peaks with both narrow linewidth (1.4 meV) and clearly splitted lineshape due to well width difference by a monolayer (ML). Black dots with error bars in Fig. 1 show the value of function F, which can be calculated only from measured PL and PLE spectra (see the right axis label of Fig. 1 for definition of F). Temperature T^* deduced from the slope of function F on the basis of KS relation shows excellent agreement with T_{env}, as was observed in doped QW in the range of 5 – 220 K [1]. This demonstrates the realization of quasi-equilibrium distribution even in an un-doped system, where the heat capacitance of carriers is considered to be quite smaller because of the absence of doped carriers.

References
[1] T. Ihara *et al.*, Phys. Rev. B **80**, 033307 (2009).
[2] E. H. Kennard, Phys. Rev. **11**, 29 (1918); B. I. Stepanov, Sov. Phys. Dokl. **2**, 81 (1957).

Authors
S. Maruyama, T. Ihara, M. Yoshita, T. Mochizuki, H. Akiyama, L. N. Pfeiffer[a], and K. W. West[a]
[a] Princeton University, USA

Direct Mapping of the Spin-Filtered Edge Modes of a Three-Dimensional Quantum Spin Hall Phase

I. Matsuda Group

Recently, theoretical frameworks of the spin-Hall effect has extended to the "quantum spin Hall" (QSH) effect, which is realized in a topologically non-trivial electronic state, as in the case of the quantum Hall effect. Edge modes of QSH carry spin currents without breaking time-reversal symmetry and they are robust against disorder, such as surface roughness or impurities. The three-dimensional (3-D) QSH phase has the edge modes of 2-D surface states and $Bi_{1-x}Sb_x$ (x=0.07-0.22) crystals have been the candidate based on the Z_2 topological band theory [1]. Previous photoemission studies [2] have mapped band dispersion curves of the (111) surface states of the semiconductor alloy

$Bi_{1-x}Sb_x$ ($x\sim$0.1) and pointed out that the crystal was the topological insulator (the 3-D QSH phase) by counting a number of the Fermi level crossing of the edge-states, which is odd for the topologically non-trivial case and even for the trivial case. However, the edge-states are theoretically spin-filtered and the complete experimental evidence has still required determination of the whole spin-polarized band structure.

In the present research, spin-polarized surface band structure of the 3-D QSH phase of $Bi_{1-x}Sb_x$ (x=0.12-0.13) was studied by high-resolution spin- and angle-resolved photoemission spectroscopy (SARPES) using our high-yield spin polarimeter [3] equipped with a high-resolution electron spectrometer, Fig. 1(a). Band dispersions of the edge-states were fully elucidated between the two time-reversal-invariant points, $\overline{\Gamma}$ and $\overline{M}$, of the (111) surface Brillouin zone [4,5], as shown in Fig. 1(b-d). The observed spin-polarized band dispersions indicate an odd number of the band-crossing at the Fermi energy, giving unambiguous evidence that this system is a 3-D QSH phase, and determine the ``mirror chirality'' to be -1, which excludes the existence of a Dirac point in the middle of the $\overline{\Gamma}$ and $\overline{M}$ line.

References
[1] C. L. Kane and E. J. Mele, Phys. Rev. Lett. **95**, 146802 (2005).
[2] D. Hsieh *et al.*, Nature **452**, 970 (2008).
[3] T. Okuda *et al.*, Rev. Sci. Instrum. **79**, 123117 (2008).
[4] A. Nishide *et al.*, Phys. Rev. B **81**, 041309(R) (2010).
[5] A. Nishide *et al.*, to be published in New J. Phys.

Authors
A. Nishide, A. A. Taskin[a], Y. Takeichi, T. Okuda, A. Kakizaki, K. Nakatsuji, F. Komori, Y. Ando[a], and I. Matsuda
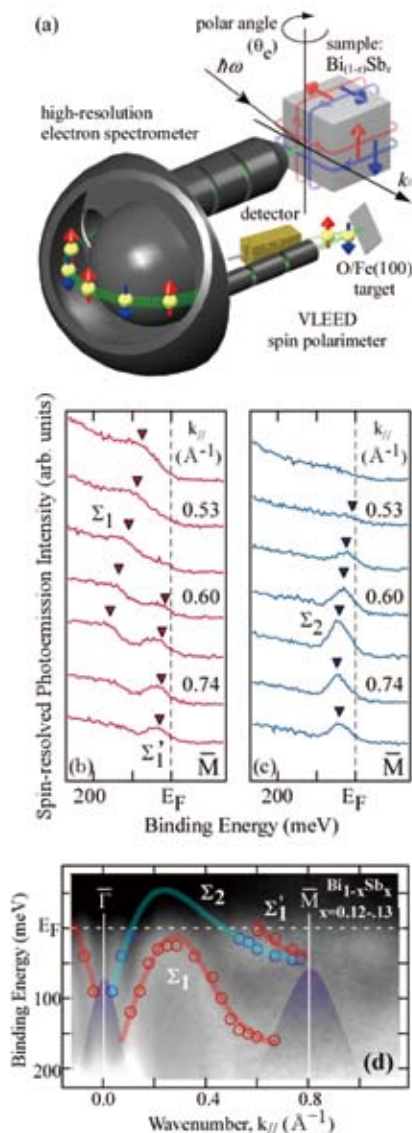[a]Institute of Scientific and Industrial Research, Osaka University

Fig. 1. (a) Schematic drawing of the high-resolution SARPES measurement. Spin-polarized electrons are depicted as red-up and blue-down arrows. SARPES spectra of (b) spin-up (red), (c) spin-down (blue) for $Bi_{1-x}Sb_x$ (x=0.12) near the $\overline{M}$ point. Peak positions of the edge-states (surface-states), Σ_1, Σ'_1, and Σ_2, are indicated. (d) Spin-polarized surface band dispersions of $Bi_{1-x}Sb_x$ (x=0.12). Spin-up (spin-down) bands are colored in red (blue) and their dispersion curves are schematically traced by thick lines. For comparison, the data are displayed on a gray-scale band diagram (x=0.13) of the spin-integrated ARPES spectra. The bulk band projection, tentatively estimated from the ARPES data, is shown as the shaded purple area.

Discovery of Novel Ferromagnetic Metal-Insulator Transition

Y. Ueda and Yagi Groups

Metal-insulator transition is one of the most drastic phenomena in strongly correlated electron systems. We found novel metal-insulator transitions in hollandites. Hollandite with a general chemical formula $A_2M_8O_{16}$ is one of minerals. The crystal structure consists of the M_8O_{16}-framework and A-cations at tunnel sites in the M_8O_{16}-framework. The most popular crystal symmetry is a tetragonal I4/m in which the crystallographycally independent M site is unique, hence, $K_2M_8O_{16}$ is a mixed valent oxide with M^{3+}/M^{4+} = 1/3. $K_2M_8O_{16}$ (M = Ti, V, Cr, Mn) have been prepared by high pressure synthesis. These compounds enable us to systematically study electron correlation effect as a function of filling level in the common band structure. $K_2Ti_8O_{16}$ at a low filling level is a Pauli-paramagnetic metal [1]. On the other hand, $K_2V_8O_{16}$ close to half-filling exhibits a metal-insulator transition accompanied by the charge ordering [2]. Very recently, we found a ferromagnetic metal-insulator transition in three-quarter-filled $K_2Cr_8O_{16}$ [3]: $K_2Cr_8O_{16}$ is a ferromagnetic metal with T_C =180 K. The net magnetization of 17.7μ_B/8Cr is very close to full moment of 18 μ_B/8Cr; $\{2Cr^{3+}(d^3) + 6Cr^{4+}(d^2)\}$. The Curie constant C = 8.1 (emu/Cr-mol)K ($\sim$7 μ_B/Cr) estimated from Curie-Weiss fitting of magnetic susceptibility in the paramagnetic region is much larger than the calculated value of 1.19 (emu/Cr-mol)K (2.25 μ_B/Cr) from the averaged
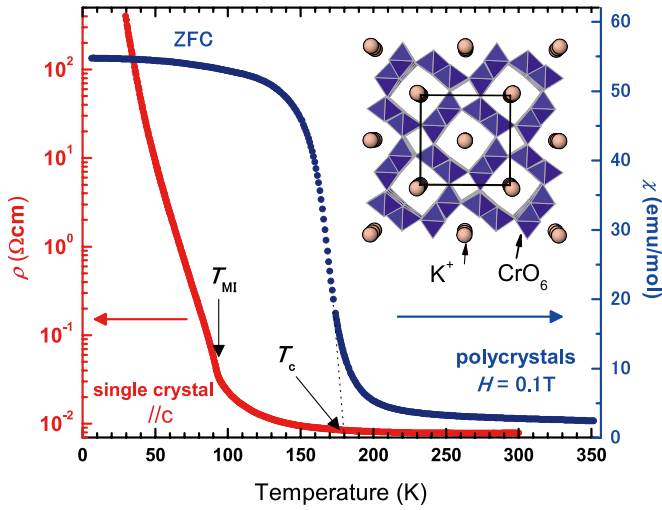
Fig. 1. Temperature dependences of resistivity (ρ) and magnetic susceptibility (χ) of $K_2Cr_8O_{16}$. $K_2Cr_8O_{16}$ is a ferromagnetic metal with $T_C =$ 180 K and shows a transition to an insulator at T_{MI} = 95 K without any apparent structural change but retaining ferromagnetism. The crystal structure consists of Cr_8O_{16}-framework and K^+-ions, as shown in the inset of Fig. 1. The Cr_8O_{16}-framework is constructed from the double-chains of edge-shared CrO_6 octahedra that are corner-connected with other chain units. It is characteristic of a one-dimensional tunnel running parallel to the tetragonal c-axis and the tunnels are filled with K^+.

valence of $Cr^{+3.75}$, which suggests strong ferromagnetic spin fluctuation. Surprisingly, this ferromagnetic metal transforms to an insulator at T_{MI} = 95 K without any apparent structural change but retaining ferromagnetism.

$K_2Cr_8O_{16}$ is quite unique in three aspects: It has a rare mixed valence of Cr^{3+} and Cr^{4+}; it has a metal (or half-metal) to insulator transition in a ferromagnetic state; and the resulting low temperature phase is a rare case of a ferromagnetic insulator. This discovery could open a new frontier on the relation of magnetism and conductivity in strongly correlated electron systems.

References
[1] M. Isobe, S. Koishi, S. Yamazaki, J-I. Yamaura, H. Gotou, T. Yagi, and Y. Ueda, J. Phys. Soc. Jpn. **78**, 114713 (2009).
[2] M. Isobe, S. Koishi, N. Kouno, J-I. Yamaura, T. Yamauchi, H. Ueda, H. Gotou, T. Yagi, and Y. Ueda, J. Phys. Soc. Jpn. **75**, 073801 (2006).
[3] K. Hasegawa, M. Isobe, T. Yamauchi, H. Ueda, J-I. Yamaura, H. Gotou, T. Yagi, H. Sato, and Y. Ueda, Phys. Rev. Lett. **103**, 146403 (2009).

Authors
Y. Ueda, M. Isobe, T. Yamauchi, H. Ueda, H. Gotou, and T. Yagi

Crossover Behavior from the 3D XY Universality in a Frustrated Magnet

Kawashima Group

$BaCuSi_2O_6$ is a quasi-two-dimensional frustrated antiferromagnet with body-centered tetragonal (BCT) lattice structure. This compound has a spin gap but it collapses in a strong magnetic field and then the system becomes magnetically ordered. As a result of symmetry of the frustrated BCT lattice, a finite temperature transition to this ordered phase breaks Z_2 symmetry in addition to the usual U(1) spin symmetry [1]. The Z_2 symmetry breaking is associated with a 90° lattice rotation.

However, an open question had been left unsettled as to the nature of this phase transition. While experimental observations suggest that the transition belongs to the 3D XY universality class, it was shown that the additional Z_2 symmetry breaking changes its nature [1]. Indeed, it had been recognized that in contrast to unfrustrated systems, the critical phenomena in certain frustrated systems can be very elusive for the standard renormalization group treatments. For example, the transition of the stacked triangular XY antiferromagnet, where the U(1)×Z_2 symmetry breaking appears as in the present case, could be a second order transition described by a "chiral" fixed point although recent numerical simulations are rather in favor of a first order transition.

Here we report on our recent numerical investigation of an effective model with the U(1)×Z_2 symmetry [2]. We consider a simple cubic lattice with two sites per unit cell. The Hamiltonian is given by

$$H = -J \sum_{\langle i, j \rangle, a=A,B} \mathbf{S}_{a,i} \cdot \mathbf{S}_{a,j} + \lambda J \sum_i (\mathbf{S}_{A,i} \cdot \mathbf{S}_{B,i})^2.$$

The sublattice A (B) contains a classical XY spin $\mathbf{S}_A$ ($\mathbf{S}_B$) coupled by the ferromagnetic interaction J. These two sublattices correspond to even- and odd-numbered layers in the BCT lattice (see Ref. [1] for details). The spins in different sublattices are only coupled by the biquadratic ferroquadrupolar interaction ($\lambda < 0$). This is the relevant interaction which drives the system away from the 3D XY fixed point $\lambda = 0$. This term tends to lock a relative phase between the A and B spins so that $\mathbf{S}_A \cdot \mathbf{S}_B = \pm 1$ in the ground state, causing Z_2 symmetry breaking at the transition.

A very efficient cluster Monte Carlo algorithm is applicable to this system, allowing for a systematic study around the unstable XY fixed point. By performing some standard
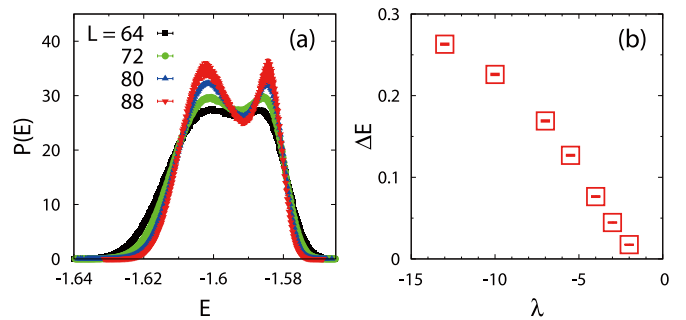

Fig. 1. (a) Bimodal energy distribution at $T \approx T_c$ for $\lambda = -2$ and (b) λ-dependence of the latent heat.
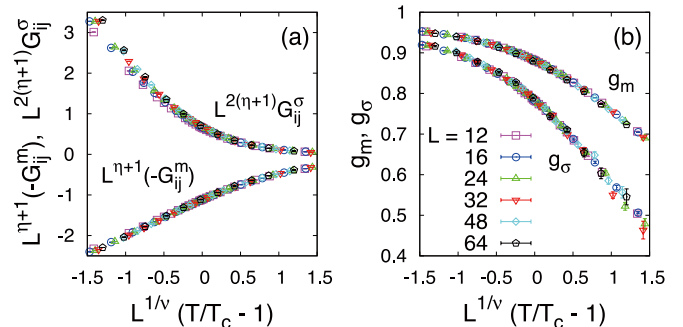

Fig. 2. (a) "Pseudo-scaling" behavior of correlation functions associated with U(1) (with superscript "m") and Z_2 ("σ") symmetry breaking with distance $r_{ij} = (L/2, L/2, L/2)$ and (b) pseudo-scaling behavior of scaling parameters called "correlation ratios," which are ratios of the correlation functions with $(L/2, L/2, L/2)$ to those with $(L/4, L/4, L/4)$. Here $\lambda = -0.05$ and η and ν are critical exponents of the 3D XY universality class.

Fig. 3. The flow diagram of dimensionless scaling parameters (6 parameters in total). (a) A three-dimensional (3D) projection onto (U_m, ξ_m/L, U_σ) space and (b–d) two-dimensional projections are shown. Because of the approximately single curve found in a four-parameter subspace (g_m, ξ_m/L, g_σ, ξ_σ/L), the analysis of the flow structure can be reduced to the 3D flow diagram. The arrows show directions of the flow lines. The estimated location of the unstable XY fixed point (U_m, ξ_m/L, U_σ) = (1.2430(5), 0.5925(2), 2.40(1)) is indicated by a large filled circle. See Ref. [2] for further details.

finite-size scaling analysis, we found that the transition is discontinuous for $|\lambda| \geq 2$ (Fig. 1), while for small $|\lambda|$ the transition is almost indistinguishable from being second order (Fig. 2).

Given this result, the question that naturally follows is whether the apparent second-order scaling behavior for small $|\lambda|$ can really be taken as an evidence of continuous nature of the transition. We performed a Monte Carlo renormalization group analysis to clarify this point and the answer turned out to be no. Figure 3 shows the numerically obtained flow diagram. Each flow line describes evolutions of several dimensionless scaling parameters with increasing system size L. Because these scaling parameters become scale-invariant at a second order transition, if there is some λ-region where the transition is continuous, corresponding flow lines must be attracted to a fixed point. However, the flow diagram clearly indicates the absence of such a stable fixed point. The flow lines systematically evolve away from the XY fixed point. Such a trend continues without making a separatrix toward the first-order region, where a flow line with $\lambda = -2$ evolves. Thus, our results strongly suggest that the transition is of the first order for any finite value of λ.

In BaCuSi$_2$O$_6$, the biquadratic interaction is expected to be extremely small because it arises from second order perturbation with respect to ratio of a very weak interlayer coupling to an intralayer coupling [1]. Therefore, even though the true asymptotic behavior is the weak first order transition, it can be observed only in a very narrow region near the transition point which could easily be beyond the standard experimental precision. The thermodynamic behavior outside this small region will be dominated by the XY fixed point, in agreement with experimental observations.

References
[1] Y. Kamiya, N. Kawashima, and C. D. Batista, J. Phys. Soc. Jpn. **78**, 094008 (2009).
[2] Y. Kamiya, N. Kawashima, and C. D. Batista, arXiv:1003.1639 (unpublished).

Authors
Y. Kamiya, N. Kawashima, and C. D. Batista[a]
[a]Los Alamos National Laboratory

Inhomogeneity-Free Tetra-PEG Gels as Revealed by Small-Angle Neutron Scattering

Shibayama Group

It is well known that polymer gels have inhomogeneous structures, such as non-uniform distribution of cross-links, dangling chains, and trapped entanglements. The inhomogeneous structures are ascribed to an introduction of cross-links to a polymeric system, which fixes the topological architecture of the system. These inhomogeneities are often characterized by an upturn in the scattering intensity at low q-region in small-angle neutron scattering (SANS) or a speckle pattern in laser light scattering, where q is the magnitude of the scattering vector. Since the physical properties of gels, such as mechanical and optical properties, strongly depend on the structure, it is extremely important to clarify the relationship between the structure and mechanical properties. The understanding of cross-link inhomogeneities is vital from both scientific and engineering points of
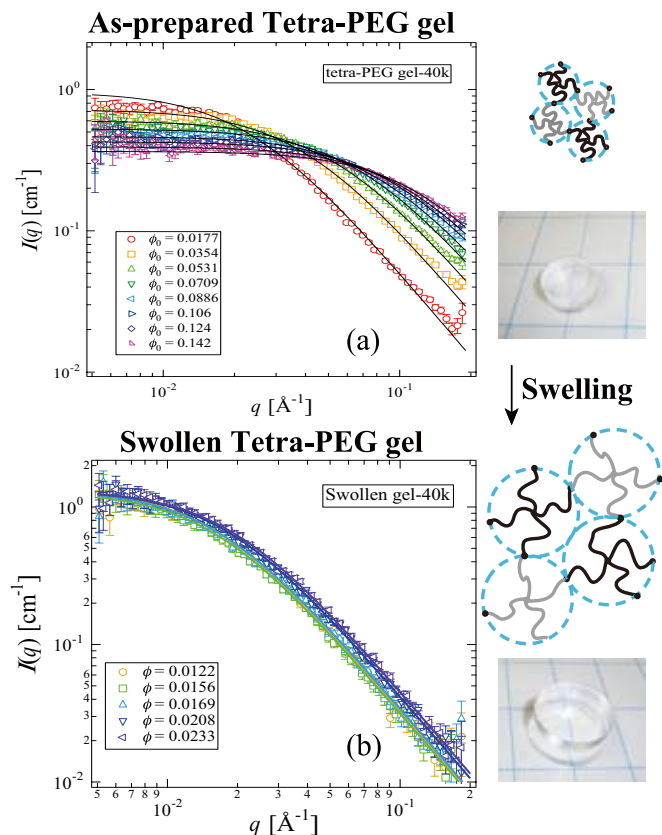

Fig. 1. SANS curves of (a) as-prepared and (b) swollen Tetra-PEG gels observed at various polymer volume fractions, ϕ_0 and ϕ, where ϕ_0 and ϕ are the volume fraction at preparation and at observation, respectively. All SANS curves are represented simply by OZ functions with the correlation length of ξ. The cartoons show the molecular architecture of Tetra-PEG gels. The photographs show as-prepared (top) and swollen gels (bottom).
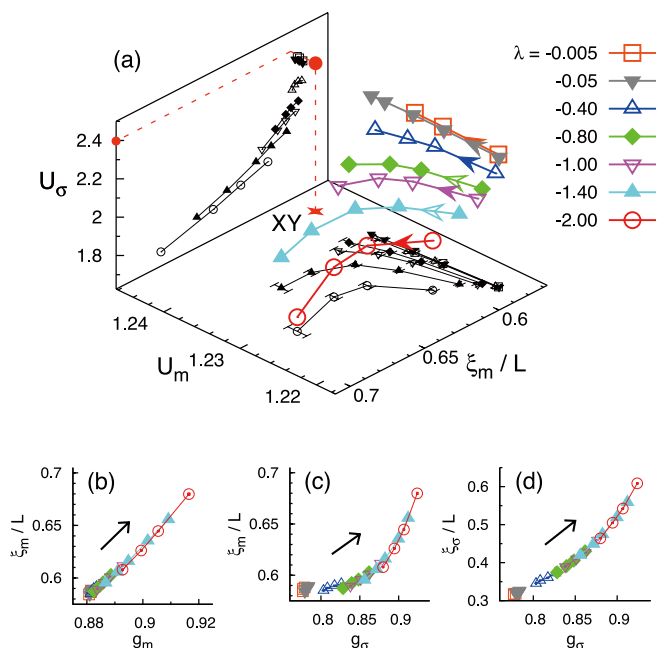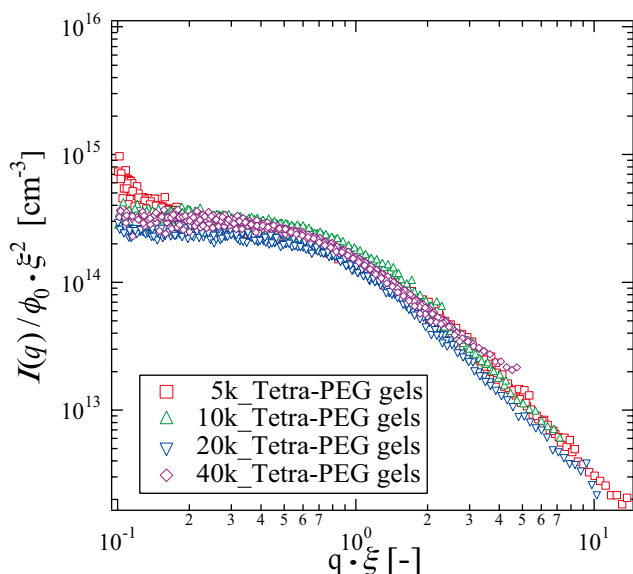
Fig. 2. SANS master curves for as-prepared Tetra-PEG gels (Mw = 5, 10, 20, and 40 kg/mol). All SANS curves can be superimposed to a single master curve by using the reduced variables of ξq and $I(q)/\phi_0\xi^2$.

view since they affect the physical properties of the network polymer, such as mechanical and optical properties. On the other hand, there has been a desire to prepare an "ideal" polymer network free from defects.

We developed a novel class of hydrogels "Tetra-PEG" gels by cross-end coupling of two-types of tetra-arm polyethylene glycol (PEG) chains [1]. The Tetra-PEG gels have various advantages, namely, high mechanical strength and toughness (stronger than cartilage), easy preparation (simple mixing of two aqueous solutions), and biocompatibility (direct implantation by injection). The Tetra-PEG gels were prepared by cross-end coupling of two types of tetra-arm PEG macromers with the molecular weights, M_w, of 5, 10, 20 and 40 × 10^3 g/mol. Interestingly, it was found that Tetra-PEG gels did not show the above-mentioned upturn behavior at low q-regions ($q > 0.01$ Å^{-1}) in SANS [2-4]. The structure factors of both as-prepared and swollen gels were represented only by Ornstein-Zernike (OZ) type scattering functions, i.e., $I(q) = I(0)/(1 + \xi^2 q^2)$, (Fig. 1) and could be superimposed to a single master curve (Fig. 2) with the reduced variables, ξq and $I(q)/\phi_0\xi^2$, irrespective of the molecular weight of tetra-PEG, where ξ, $I(q)$, and ϕ_0 are the correlation length, the scattering intensity, and the polymer volume fraction at preparation, respectively. The SANS curves for swollen gels were independent of ϕ (the polymer volume fraction at observation), indicating that Tetra-PEG gels are entanglement-free model networks. We then concluded that the extraordinary toughness of Tetra-PEG gels was ascribed to a "perfect" and "ideal" network like a diamond-like tetrahedral structure.

References
[1] T. Sakai, T. Matsunaga, Y. Yamamoto, C. Ito, R. Yoshida, S. Suzuki, N. Sasaki, M. Shibayama, and U. Chung, Macromolecules **41**, 5739 (2008).
[2] T. Matsunaga, T. Sakai, Y. Yamamoto, Y. Akagi, U. Chung, and M. Shibayama, Macromolecules **42**, 1344 (2009).
[3] T. Matsunaga, T. Sakai, Y. Akagi, U. Chung, and M. Shibayama, Macromolecules **42**, 6245 (2009).

Authors
T . Matsunaga, T. Sakai, Y. Akagi, U. Chung, and M. Shibayama

Glass Transitions and Low-energy Excitations of Vapor-deposited Simple Molecular Glasses

Yamamuro Group

There remain many unsolved problems in the physical properties of glasses, *e.g.*, glass transitions, boson peaks, beta relaxations, etc. One of the essential approaches to these problems is to study molecular glasses with simple molecular structures such as rare gas and diatomic molecules. This study enables us to make direct comparison with the results of various theoretical and computer simulation studies. The best method to realize simple molecular glasses is a vapor-deposition at low temperature. Its quenching rate is roughly estimated to be more than 10^7 Ks^{-1}. Recently, we have developed a novel adiabatic calorimeter for vapor-deposited samples. This calorimeter enables us to deposit sample vapor on the inside surface of the cell at ca. 10 K and do in situ heat capacity measurements from 2 K. By using this calorimeter, we have realized the glassy carbon tetrachloride (CCl$_4$) and propene (CH$_2$=CHCH$_3$), both of which have simple molecular structures without any intramolecular conformational change.
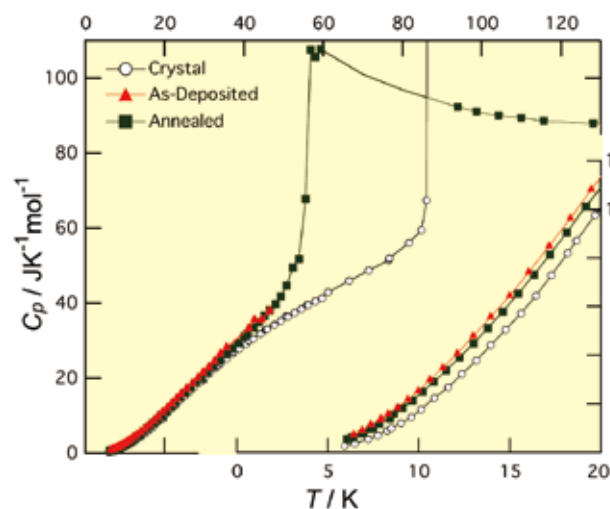

Fig. 1. Heat capacities of propene in crystalline, as-deposited glassy and annealed glassy states. The annealed sample was prepared by annealing the as-deposited one around the glass transition temperature 56 K.
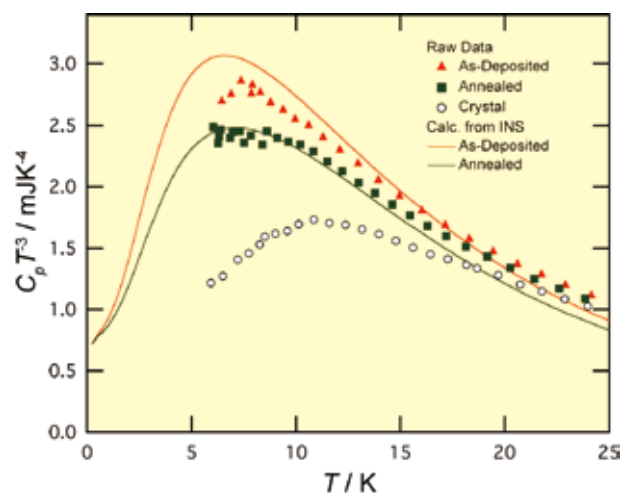

Fig. 2. Heat capacities divided by cubic temperature, roughly corresponding to the density of states divided by squared temperature. The data calculated from the density of states obtained by inelastic neutron scattering are given for comparison.

On heating the glassy carbon tetrachloride and propene, the former crystallized at 50 K while the latter exhibited a glass transition at 56 K. Figure 1 shows the heat capacities of crystalline and glassy propene. A large jump of heat capacity was observed at the glass transition temperature T_g. The analysis of configurational entropy revealed that the size of the cooperatively rearranging region (CRR) of supercooled propene becomes larger as decreasing temperature and reaches about ten molecules at T_g. Comparing this result with those of other hydrocarbon glasses studied so far, we have found that the CRR size at T_g is correlated with the inverse of molecular mass. Figure 2 shows the heat capacities divided by cubic temperature T^3, roughly corresponding to the density of states devided by T^2. The Debye term will become constant in this plot. The glassy samples exhibit excess heat capacities reflecting the low-energy excitations, usually called boson peaks. The boson peak intensity of the as-deposited sample is larger than that of the annealed one. This result is quite consistent with the previous inelastic neutron scattering data shown by the curves in Fig. 2. These data strongly indicate that the origin of the boson peak is associated with the structural disorder and distortion relaxed by the annealing. Further analyses on the CRR and boson peak are now going on.

Authors
S. Tatsumi, S. Aso, and O. Yamamuro

Inelastic Neutron Scattering Study on the Triangular Spin Cluster V₃

Sato Group

As the size of a spin system decreases, the quantum aspects of the system emerge out of well-known macroscopic classical behavior. Molecular nanomagnets provide an excellent playground to experimentally investigate such quantum aspects of finite-sized spin systems as they consist of small spin clusters magnetically isolated by ligands from other clusters. Various intriguing quantum phenomena have been observed in molecular nanomagnets to date, and one of such intriguing phenomena may be the half-step magnetization change in the triangular spin clusters with $s = 1/2$.

As each spin has $s = 1/2$, the total spin of three antiferromagnetically coupled spins can be either $S = 1/2$ or $S = 3/2$, and thus the magnetization step should be $S^z = 1/2$ -> $3/2$ (i.e., integer magnetization step in S^z.) Therefore, it was a big surprise when the magnetization experiment detects half-step magnetization in the V₃ triangular spin cluster. Soon after the observation of the half-step magnetization, an perturbative term, the Dzyaloshinsky-Moriya(DM) interaction, in the spin Hamiltonian is theoretically suggested to be the key ingredient for this non-trivial quantum phenomenon. However, the experimental determination of the model Hamiltonian was not complete, and thus we here have undertaken the neutron inelastic scattering study on the V₃ triangular spin cluster (chemical formula: K₁₁H[(VO)₃(SbW₉O₃₃)₂].27H₂O) [1].

The high-resolution neutron inelastic scattering experiment has been performed using the ISSP-HER triple-axis spectrometer installed at the C1-1 port of the cold guide tube, JRR-3, Tokai, Japan. The 0.7 grams of deuterated powder sample was used in the experiment. The energy resolution at
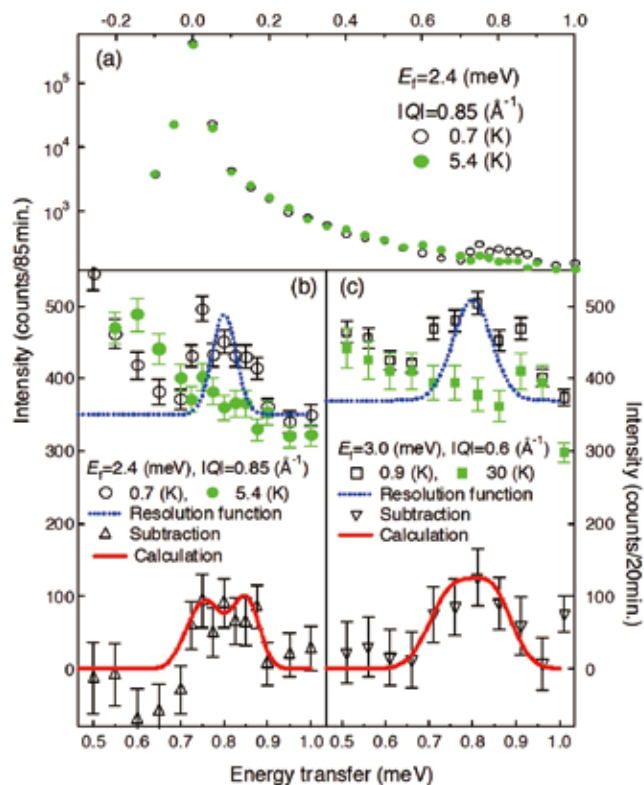

Fig. 1. (a) Inelastic neutron scattering spectra at $|Q| = 0.85$ Å^{-1}, and at $T = 0.7$ K (Open circle) and 5.4 K (Green). (b, c) Magnified figures for $0.5 < \hbar\omega < 1.0$ meV region with $E_f = 2.4$ and 3.0 meV, respectively. The bottom figures stand for the temperature difference between the lowest and the sufficiently higher temperatures to show the magnetic contributions. The blue dashed lines represent the instrumental resolution, whereas red solid lines stand for the resolution-convoluted calculated scattering function $S(Q, \hbar\omega)$.

the elastic position was estimated as $\Delta\hbar\omega = 49$ or 89 μeV for the $E_f = 2.4$ meV or 3.0 meV mode, respectively.

Figure 1 shows the representative inelastic scans at $|Q| = 0.85$ Å^{-1} and $|Q| = 0.6$ Å^{-1}. The top panel shows the spectrum in the full log scale, whereas the bottom panels show the inelastic-peak region only. A broad inelastic peak, centered at $\hbar\omega = 0.8$ meV, can be clearly seen in the spectrum at the lowest temperature, whereas it disappears at the higher temperatures. The temperature difference (shown at the bottom) clarifies the magnetic nature of this inelastic scattering component.

From the detailed analysis of $\hbar\omega$- and Q-dependence of the inelastic peak intensity (not only the peak positions), we concluded that the spin Hamiltonian consists of site-independent anisotropic exchange parameters J^α ($\alpha = x, y, z$) and site-dependent DM interactions D^α_{ij} as:

$J^x = J^y = -5.7$ K,

$J^z = -6.8$ K,

$D^z_{1,2} = 0.26$ K,

$D^z_{2,3} = D^z_{3,1} = 0.28$ K,

where i (j) stands for the site index. Our analysis confirms the existence of the DM interaction in the V₃ triangular spin cluster, and thus supports the idea that the DM interaction is the origin of the half-step magnetization change in this material.

The other important aspect is that through this study we have developed a general analysis technique to obtain parameters of the model Hamiltonian by fitting $S(Q, \hbar\omega)$. We utilize not only the peak position but also the intensity information; this method will bring about a drastic improvement in the parameter determination using neutron inelastic

scattering. Several other molecular nanomagnets are under investigation to confirm the validity of this new analysis method.

Reference
[1] K. Iida, H. Ishikawa, T. Yamase, and T. J. Sato, J. Phys. Soc. Jpn. **78**, 114709 (2009).

Authors
T. J. Sato and K. Iida

Observation of Strong Magnetoelectric Coupling in Multiferroic BiFeO$_3$ above Room Temperature

Tokunaga Group

Recently, ferroelectric magnets, *i.e.* so-called multiferroic materials, have attracted considerable attention due to their richness of scientific interests and also potential application for novel memory devices with reduced power consumption. In this class of materials, most of the attractive phenomena are caused by the presence of strong coupling between the magnetic moment and the electric polarization (P). In general, the coupling between them cannot be strong because these two order parameters have different symmetry against time reversal and space inversion operation, and hence, do not have a linear coupling term in the expression of the free energy. This constraint is removed in some kinds of magnets with spatially modulated spin structures (SMSSs), in which spatial inversion symmetry is broken by the magnetic order [1,2]. Since such SMSSs usually originate from geometrical frustration in the spin system, the strong magnetoelectric coupling emerges only at low temperatures. In this context, BiFeO$_3$ is the unique example that shows multiferroic nature above room temperature with large electric polarization of P ~ 100 μC/cm^2 [3,4].

We studied the effect of magnetic fields on BiFeO$_3$ using single domain crystals grown by the flux method [5]. At low temperatures, metamagnetic transitions accompanied with steep changes in P take place at magnetic fields of ~ 19 T along the [100] direction of the pseudocubic lattice. Magnetic torque measurements in various field-directions show that the transition field becomes the highest when the magnetic field is applied along the [111] direction (Fig. 1). This angular dependence is reproduced by a phenomenological argument based on the Ginzburg-Landau theory, which indicates this transition to be a magnetic one from the cycloidal to the canted antiferromagnetic state. According to the recent microscopic theory [1], this change in the spin structure is accompanied with the disappearance of the parasitic P caused by the SMSS.

We studied temperature dependence of this parasitic component through the measurements of the field-induced change in P (ΔP) up to 500 K (Fig. 2). The transition field decreases with increasing temperature toward the Néel temperature of ~ 600 K, whereas the magnitude of the ΔP remains greater than 100 μC/m^2 up to 450 K. Although this value is much smaller than that of the spontaneous polarization, it is comparable to those in other multiferroic materials. In particular, the evaluated microscopic coupling constant between the spin and electric polarization is even larger than that in the standard multiferroic material of TbMnO$_3$.
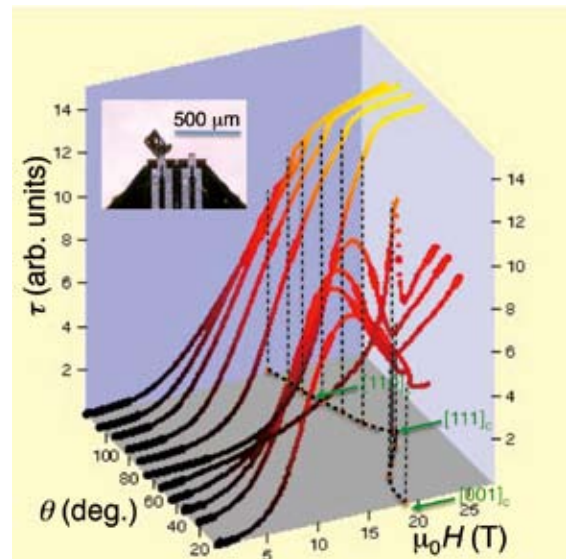

Fig. 1. Magnetic field dependence of magnetic torque (τ) measured with using a micro-piezoresistive cantilever in various field directions at T = 4.2 K. The field direction was changed from the [001] to the [110] axis in the cubic notation. The transition field becomes the highest when the field is applied along the [111] direction. The thick dotted line schematically shows the calculated transition field based on the Ginzburg-Landau theory. The coincidence with the experimental results indicates the validity of this argument.
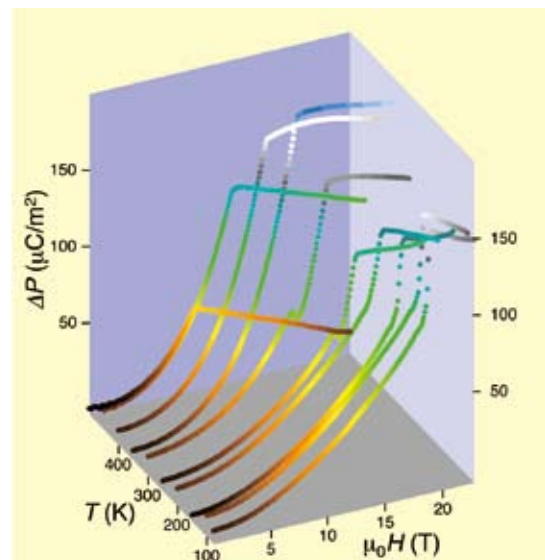

Fig. 2. Magnetic field-induced changes in P (ΔP) projected to the cubic [001] direction at various temperatures from 77 K to 500 K. Magnetic fields were applied perpendicular to the projection axis. The transition field becomes smaller with increasing the temperature toward the Néel temperature of ~ 600 K. The field-induced change in P remains larger than 100 μC/m^2 up to 450 K.

The present finding of the strong magnetoelectric coupling in BiFeO$_3$ provides a strategy to design novel multiferroic materials of practical use.

References
[1] H. Katsura, N. Nagaosa, and A. V. Balatsky, Phys. Rev. Lett. **95**, 057205 (2005).
[2] M. Mostovoy, Phys. Rev. Lett. **96**, 067601 (2006).
[3] V. V. Shvartsman *et al.*, Appl. Phys. Lett. **90**, 172115 (2007).
[4] D. Lebeugle *et al.*, Appl. Phys. Lett. **91**, 022907 (2007).
[5] M. Tokunaga *et al.*, J. Phys. Soc. Jpn. **79**, 064713 (2010).

Authors
M. Tokunaga, M. Azuma[a], and Y. Shimakawa[a]
[a] Institute for Chemical Research, Kyoto University

X-ray Magnetic Circular Dichroism of Valence Fluctuating Eu in High Magnetic Fields of up to 40 T

Y. Matsuda Group

In high magnetic fields, various kinds of intriguing phenomena such as magnetic, electronic and structural phase transitions are observed in some strongly correlated electron systems. Synchrotron x-rays are powerful and important microscopic probes for the field-induced phenomena. Other microscopic measurement techniques such as the photoemission spectroscopy and scanning tunneling microscopy are very difficult to perform in high magnetic fields over 30 T where a commercial superconducting magnet is not available.

X-ray magnetic circular dichroism (XMCD) spectroscopy is one of the most powerful tools to study the electronic and magnetic states with the element- and shell-selectivity. Although there have been a lot of excellent works on the XMCD of the magnetic materials, most of them are the studies on ferromagnetic materials. This is partly because high magnetic fields were not available at synchrotron x-ray facilities.

In the present work, we have made the XMCD experiment of the Eu-based valence fluctuating compounds in high magnetic fields of up to 40 T using pulsed magnetic fields. A miniature magnet and a portable type capacitor bank that were developed recently by our group [1, 2] are used for generation of pulsed fields. The experiment was carried out at BL39XU in SPring-8.

The measured XMCD spectra of $EuNi_2(Si_{0.82}Ge_{0.18})_2$ are shown in Fig. 1 together with the XAS spectra at several magnetic fields [2]. Here we only show the L_2 edge spectra. The valence fluctuation manifests itself as a double-peak structure in the XAS spectra. The higher energy XAS peak is attributed to the Eu^{3+} state, while the lower energy peak is attributed to the Eu^{2+} state. The XAS spectrum strongly depends on the magnetic field, exhibiting a valence change induced by the magnetic field. We found that the double-peak structure corresponding to the two valence states is observed in the XMCD spectra as well as in the XAS spectra. The double peaks indicate that the electrons in the Eu 5d orbital, where the excited electron finally goes in the
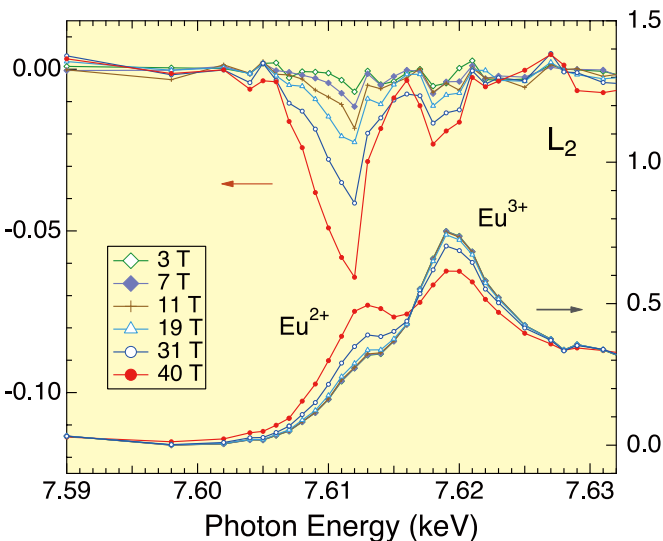

Fig. 1. X-ray magnetic circular dichroism (XMCD) and X-ray absorption spectra at different magnetic fields. The measurement temperature is 5 K.
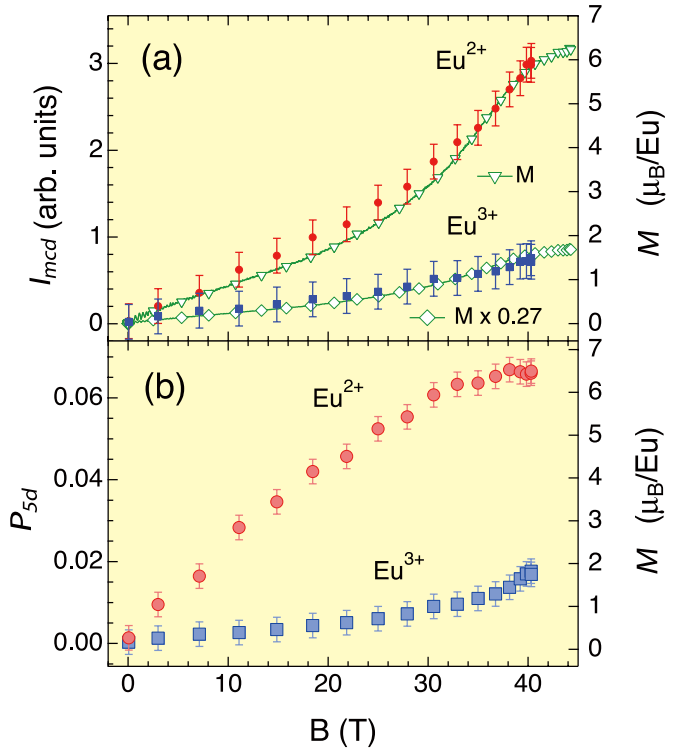

Fig. 2. Magnetic field dependence of the integrated intensity of the XMCD peak (I_{mcd}) and that of the degree of the magnetic polarization (P_{5d}). The magnetization curves are also shown for the comparison.

$L_{2,3}$ transitions, are magnetically polarized not only in the Eu^{2+} state (f^7; $J = 7/2$ in the ground state), but also in the Eu^{3+} state (f^6; $J = 0$ in the ground state). We also observed similar double peak structure in the L_3-edge XMCD spectra [3]. It is worth noting that it is nontrivial why we have a finite XMCD signal for the nonmagnetic Eu^{3+} state.

In order to clarify the origin of the valence-selective XMCD, we plot the field dependence of the integrated intensity of the XMCD peak (I_{mcd}), as well as the magnetic polarization of the 5d electrons (P_{5d}) in Fig. 2. P_{5d} in each valence state is defined here as the normalized XMCD intensity by the absorption intensity [3]. The magnetization (M) of the sample at 4.2 K [4] is also shown in Fig. 2 in order to compare it with the dependence of I_{mcd} and P_{5d} on the field. An increase of the magnetization caused by the valence change is observed at around 35 T. In addition, I_{mcd} of Eu^{2+} and that of Eu^{3+} scale together with the magnetization, as expected for XMCD experiments. However, P_{5d} is qualitatively different for the Eu^{2+} and Eu^{3+} states, suggesting the different origin of the XMCD for each valence state.

We have now possible two explanations of the valence-selective Eu^{3+}-XMCD; (i) effect of the excited state Eu^{3+} ($J = 1$), and (ii) magnetic polarization of the conduction electrons through the c-f hybridization. Since the first excited state of Eu^{3+} is magnetic ($J = 1$), the first possible origin (i) should have some effects. The energy separation between the first excited and ground states is about 480 K. If we take the Van Vleck term of Eu^{3+} into account, the contribution of the magnetization is found to be too small to explain the experimental result [3]. However, in compounds exhibiting valence fluctuation, the mixing between the Eu^{3+}: $J = 0$ and Eu^{3+}: $J = 1$ states can be enhanced by the strong c-f hybridization. Therefore, the effect of Eu^{3+}: $J = 1$ state is one of the plausible origins of the Eu^{3+}-XMCD observed in the present work. The second possible origin is that the conduction electrons are polarized by the strong hybridization with the 4f electrons in the magnetic Eu^{2+} states, and these polar-

ized conduction electrons induce the magnetic polarization of the 5d electrons in the nonmagnetic Eu^{3+} state. Owing to the strong c-f hybridization, this mechanism is also regarded as a plausible one. Although further studies are required to quantitatively understand the valence-selective XMCD, it is likely that the c-f hybridization strength plays an important role. It is expected that the high-field XMCD spectroscopy sheds new light on the problem of the strong correlation between the conduction and localized electrons.

References
[1] Y. H. Matsuda et al., J. Phys. Soc. Jpn. **75**, 024710 (2006).
[2] Y. H. Matsuda et al., J. Phys. Soc. Jpn. **76**, 034702 (2007).
[3] Y. H. Matsuda et al., Phys. Rev. Lett. **103**, 046402 (2009).
[4] H. Wada et al., J. Phys. Condens. Matter **9**, 7913 (1997).

Authors
Y. H. Matsuda, Z. W. Ouyang [a], H. Nojiri [a], T. Inami [b], K. Ohwada [b], M. Suzuki [c], N. Kawamura [c], A. Mitsuda [d], and H. Wada [d]
[a] IMR, Tohoku Univ.
[b] JAEA/SPring-8
[c] JASRI/SPring-8
[d] Kyushu University